Award Number: W81XWH-11-1-0752

TITLE: Mechanism and Therapy for the Shared Susceptibility to Migraine and Epilepsy After Traumatic Brain Injury

PRINCIPAL INVESTIGATOR: Kevin C. Brennan M.D.

CONTRACTING ORGANIZATION: University of Utah

Salt Lake City, UT 84112-9023

REPORT DATE: October 2014

TYPE OF REPORT: Annual

PREPARED FOR: U.S. Army Medical Research and Materiel Command, Fort Detrick,

Maryland 21702-5012

DISTRIBUTION STATEMENT: Approved for Public Release; Distribution Unlimited

REPORT DOCUMENTATION PAGE

1. REPORT DATE	2. REPORT TYPE	3. DATES COVERED
October 2014	Annual	30Sep2013 – 29Sep2014

4. TITLE AND SUBTITLE

Mechanism and Therapy for the Shared Susceptibility to

Migraine and Epilepsy After Traumatic Brain Injury

5a. CONTRACT NUMBER

5b. GRANT NUMBER
W81XWH-11-1-0752

5c. PROGRAM ELEMENT NUMBER

6. AUTHOR(S)

Kevin C. Brennan, Ed Dudek, Wendy Pouliot, Jorge Manuel Mendez
Punam Sawant, Dan Kaufmann

E-Mail: k.c.brennan@hsc.utah.edu

5d. PROJECT NUMBER

5e. TASK NUMBER

5f. WORK UNIT NUMBER

7. PERFORMING ORGANIZATION NAME(S) AND ADDRESS(ES)

University of Utah
383 Colorow Drive, Room 364
Salt Lake City UT 84108

8. PERFORMING ORGANIZATION REPORT NUMBER

9. SPONSORING / MONITORING AGENCY NAME(S) AND ADDRESS(ES)

U.S. Army Medical Research and Materiel Command
Fort Detrick, Maryland 21702-5012

10. SPONSOR/MONITOR'S ACRONYM(S)

11. SPONSOR/MONITOR'S REPORT NUMBER(S)

12. DISTRIBUTION / AVAILABILITY STATEMENT

Approved for Public Release; Distribution Unlimited

13. SUPPLEMENTARY NOTES

14. ABSTRACT

Our proposal studies the natural history and mechanisms of increased brain excitability leading to migraine and epilepsy after traumatic brain injury. In the 30 months since this grant was funded, we have completed experiments spanning nearly the whole range of our proposed work. The most important milestones in this project year have been: 1. Continued successful implementation of very challenging *post-TBI in vivo* two-photon imaging and *in vivo* whole cell recording, with manuscript in preparation of *novel TBI-specific phenotypes* from our *in vivo* whole cell recordings. 2. Novel findings from two-photon recordings. 3. Novel findings from recording of acute and chronic remote telemetry datasets. 4. Progressive implementation of histological techniques. 5. Collection of post-TBI behavioral datasets. 6. Publication of the preliminary data for this grant in *Stroke.*

15. SUBJECT TERMS

Traumatic brain injury, cortical spreading depression, seizure, post-traumatic headache, post-traumatic epilepsy, migraine, epilepsy.

16. SECURITY CLASSIFICATION OF:			17. LIMITATION OF ABSTRACT	18. NUMBER OF PAGES	19a. NAME OF RESPONSIBLE PERSON USAMRMC
a. REPORT	**b. ABSTRACT**	**c. THIS PAGE**			
U	U	U	UU	34	**19b. TELEPHONE NUMBER** *(include area code)*

2

TABLE OF CONTENTS

INTRODUCTION

Despite great improvements in medical care, traumatic brain injury (TBI) remains the leading cause of death in those under 40 years of age[1,2], in both civilian and military populations. Moreover, as protective strategies and acute treatment have improved, TBI survivors are often profoundly affected by the long-term consequences of injury. These long-term consequences include two disorders of altered brain excitability: chronic headache (usually chronic migraine) and epilepsy. Our proposal examines the links between TBI and these two conditions, which themselves are closely related[3] and can occur in the same patient after injury. Our underlying hypothesis is that the shared susceptibility to migraine and epilepsy after TBI is due to a long-term increase in cortical excitability induced by brain trauma.

Specifically:

-We suspect that the secondary injury phase after TBI, characterized by edema, excitation, and profound structural changes, entrains a 'negative' plasticity, which results in long-term aberrant excitation. We test this with prospective monitoring and mechanism-driven experimental manipulation.

-It is our hypothesis that the glial scar serves as a nidus of hyperexcitability even after conventional recovery is complete. We test with video EEG monitoring for increased excitability, and use behavioral measures to test the pain response. We will specifically probe the glial scar and surrounding tissue for evidence of aberrant excitation.

-If development of migraine and epilepsy after TBI is driven by cortical plasticity, modulation of these processes is important, but clinical tolerability is crucial. Memantine is both well tolerated and mechanistically promising; we will test it after CCI as a potential preventive of post-traumatic migraine and epilepsy.

BODY

Specific Aim 1
Determine whether TBI causes a self-perpetuating increase in excitability that sets the stage for epilepsy or chronic migraine

Major Task 1. Acute/subacute experiments after controlled cortical impact (CCI) TBI (Brennan, Dudek, Months 1-48)

Subtask 1:
**Perform CCI, implant monitoring device, and monitor for acute/subacute effects of TBI (7 days after injury)**

Dudek Lab CCI Procedure.
Male, C57B1/6 mice (n=29) were anesthetized with 2-4% isofluorane and pretreated with atropine (2 mg/kg), and penicillin (0.2 mL, SC, 300,000 IU). The surgical site was shaved, prepped with betadine scrub and solution and isolated with sterile surgical towels. For the CCI procedure, once the mouse was secured in the stereotaxic unit, a rectal probe was inserted and a rectal temperature of 37 ± 0.5 °C was maintained with a temperature-controlled heating pad. Next, a mid-sagittal skin incision was made from the occipital notch to the forehead. A dental drill was used to perform a 3-mm craniotomy, using bregma, and coronal, lambdoidal, and interparietal sutures as landmarks. A microprobe (Physiotemp) was inserted through a burr hole into the left frontal cortex to monitor brain temperature, which was maintained at 37 ± 0.5 °C by adjusting the warming blanket and warming lights. For the injury 1-mm metal impactor tip was pneumatically driven at a velocity of 4.0 m/s, depth of pentration 1.0 mm and duration of 100 msec to induce the traumatic brain injury. For the EEG recordings 2 holes were drilled into the skull for the support screws and the two wire EEG electrodes placed on the dura over the CCI-injury site. The entire electrode unit was secured to the skull with dental cement. The skin surrounding the electrode base was sutured shut with non-dissolvable suture. Bupivicane (7.5mg/ml, SC) was applied to all surgical sites. Age-matched sham craniotomies served as controls. Shams underwent anesthesia and preparative surgery but no CCI.

Seizures after CCI TBI.
To continue testing the hypothesis that acute seizures following a traumatic brain injury may be a predisposing factor for the development of PTE, we subjected mice (n=15) to a moderately severe CCI injury. Immediately after the impact, the mice were implanted with a wireless EEG telemetry device. To serve as a control, sham-operated mice (n=14) underwent the same surgical procedures but were not injured. Video-EEG data were collected continuously for 90 days. To date, we have analyzed 30 of the 90 days of video-EEG recordings. Thus far, we have recorded spontaneous seizures in 26% (4/15) of the CCI-injured mice. Nine hours post-injury, one mouse developed status epilepticus (**Figure 1**) which continued for 3 days resulting in the animal's death. Spontaneous recurrent seizures were recorded in 3 other CCI-injured mice (**Figure 2**). For the CCI-injured mice, the average seizure frequency was 0.10 seizures per day.
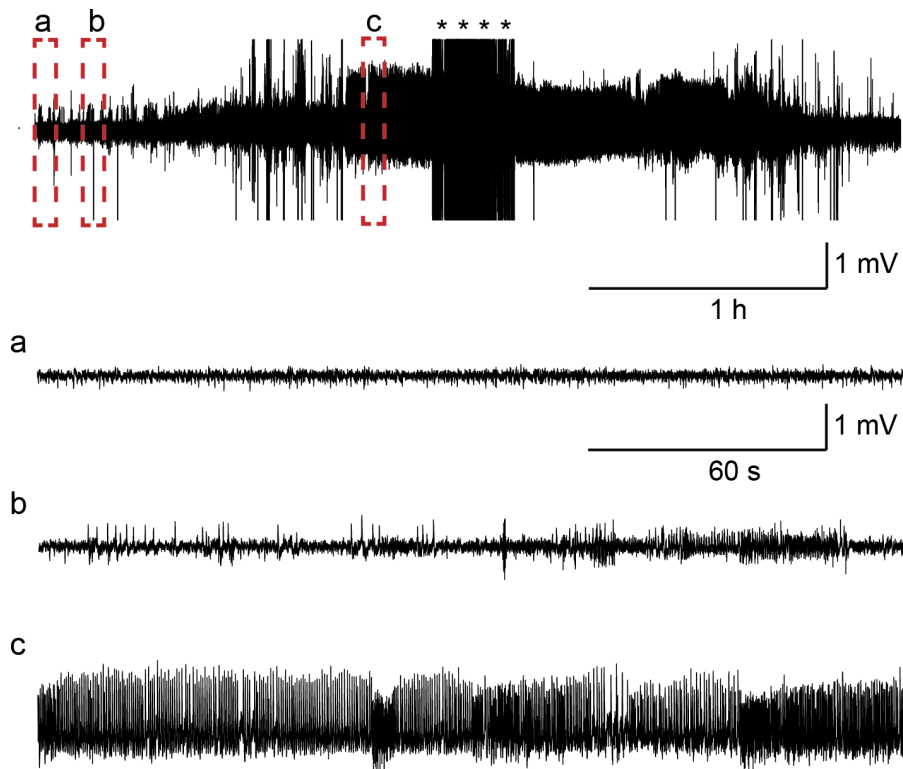
Figure 1: *Electrographic recording of a CCI-injured mouse in status epilepticus.*
*Upper trace is an EEG recording of 4 h of status epilepticus while the lower traces represent portions of the EEG within the dashed boxes at an expanded timescale. The recordings below demonstrate the baseline EEG (a), an individual seizure (b) and the continuous spiking evident of status epilepticus (c). * represents movement artifact from the seizure motor activity.*

Although we have successfully recorded spontaneous seizures from CCI-injured mice for 90 days, four potential caveats exist. The first is that the incidence of seizures in the CCI-injured mice was low (26%). In order to test the effects of memantine on the development of post-traumatic epilepsy, we may have to increase both the incidence of seizures and seizure frequency in the experimental group. As is evident clinically, the time from the injury to the development of late spontaneous recurrent seizures can be lengthy and variable. In order to maximize our ability to detect late seizures, we can length the time of EEG recordings from 90 to 120 days.

The second caveat is that early or subacute seizures were recorded from 21% of the sham-operated controls (**Figure 3**). Seizure/epileptiform activity in sham-operated controls has been reported by others[4]. Clinically, a risk factor for developing epilepsy is having undergone a craniotomy. Craniotomies themselves can produce neuronal damage[5]. To reduce the incidence of subacute seizures in our control group, we can change our methods for the craniotomy. Currently, we are using a dremel with a round burr attachment to perform the craniotomy. There is evidence to suggest that a stereotaxic mounted trephine with cold-saline irrigation can reduce the amount of neuronal damage resulting from the craniotomy[5]. Therefore, we can implement this new method to reduce the underlying damage from the craniotomy and thus reduce the incidence of seizures in the control group. Alternatively, the control group could include a sham operation without the 3 mm craniotomy.
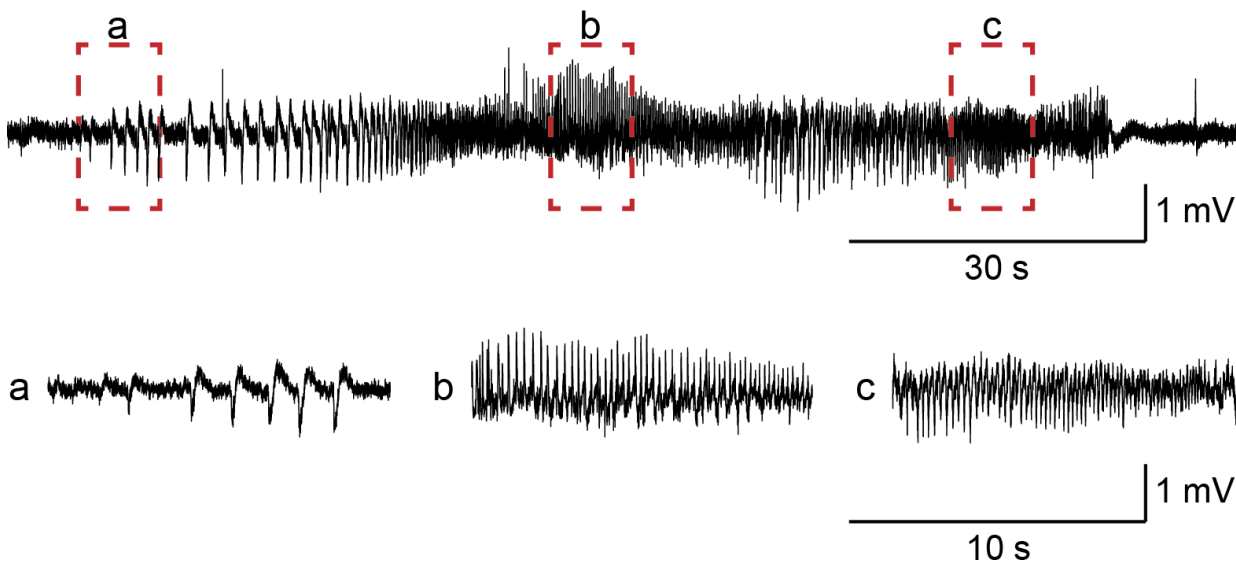
Figure 2: *A spontaneous recurrent seizure in a CCI-injured mouse. An example of an electrographic seizure recorded from a CCI-injured mouse 28 days after the injury. The EEG traces below were selected from the areas highlighted by the dashed boxes. Illustrated in an expanded time scale is the spiking pattern from the beginning (a) middle (b) and end (c) of the seizure.*

The third caveat is that the mortality in the CCI-injured mice was 46%. The majority of the mortality occurs within 1 week following the injury. Although this mortality rate is similar to what has been reported in other TBI studies with moderate-severe injury, we can work to minimize this. To minimize mortality, we can either alter the depth of the injury or adjust the location of the impact.

The fourth caveat is that we lost EEG recordings over time in both the sham-operated and CCI-injured mice (Figure 3). A loss of the EEG recording (33% in the CCI-injured group) resulted from either a loss of the recording electrode from the animal's head or a dead battery in the unit. To minimize the loss of recording electrodes, we can secure the unit to the animal's head with an additional support screw. Although the animals are implanted with units containing a 6-month battery life, the units can fail prematurely. We are working with the supplier to insure that the units will have the appropriate battery life to complete the study.
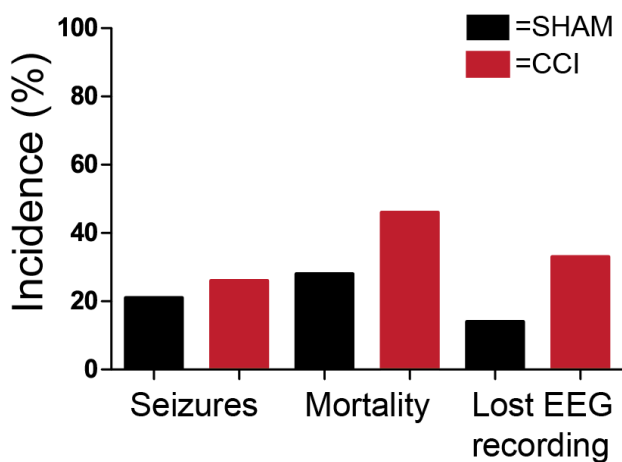
Figure 3: *Bar graph showing the incidence of seizures, mortality and loss of EEG recordings in both the sham-operated controls and CCI-injured mice.*

Seizures and possible cortical spreading depression (CSD) after CCI TBI.
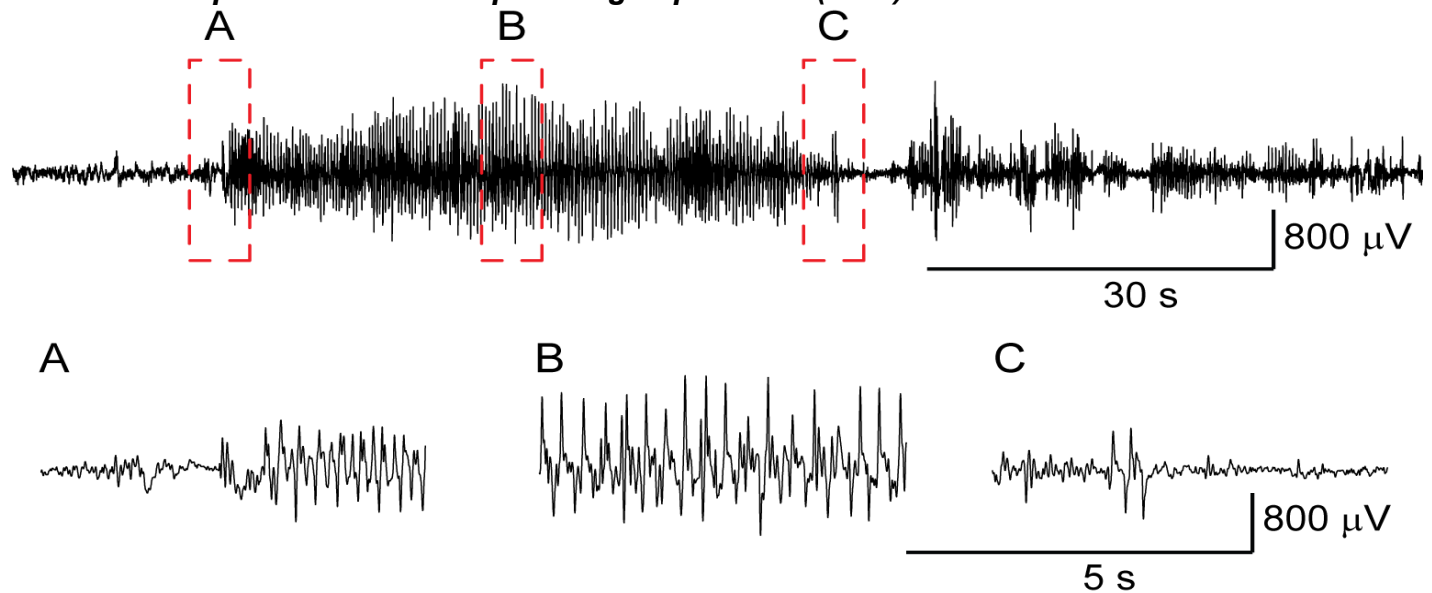

Figure 4: An example of an electrographic seizure recorded from a CCI-treated rat recorded 3 days post CCI injury. The traces below are expansions of the EEG located in the red dashed boxes. Temporal progression of the beginning (A) middle (B) and end of the seizure (C).

In a separately funded study we have been recording in rats after CCI. These animals are shown because they demonstrate a long-lasting EEG suppression that resembles what would be seen in an alternating current (AC) recording of cortical spreading depression. In this study, experimental animals (n=5) underwent similar CCI procedures to mice, scaled up for rat, while control animals (n=5) underwent a craniotomy and EEG electrode implantation only. Video-EEG data was recorded within 30 min of the injury and for 3-7 days post CCI-injury with a tether-based EEG recording setup. In the majority of the CCI-injured rats, the background EEG signal was suppressed for several hours (see **Figure 4c**). This suppression in background EEG may be caused by spreading depression. Subacute seizures were observed in 40% of rats (see **Figure 4a,b**). We are currently analyzing our mouse data to detect this phenotype. Preliminarily, we do not detect it as robustly as in rat; one difference in preparation that may be relevant is that rats were recorded with a tethered system which has a high pass cutoff (low frequency range) broader than the wireless telemetry devices we are using in mice.

Subtask 2. Perform CCI, thresholding for seizure, cortical spreading depression.

Brennan Lab CCI Procedure.
The Leica Impact One steroteaxic impactor [6] was purchased and tested for its reproducibility of impact parameters. The settings used for all experiments thus far have been the following: 4 m/s velocity, 100 ms dwell time, 1 mm impact depth. We have been using a 1 mm diameter flat tipped impactor. So far the device has worked flawlessly, and 2 mm craniotomy surgeries have been very successful (see **Figure 5**). Thus far, 67 animals have undergone CCI; 15 have undergone sham procedure (craniotomy without CCI).
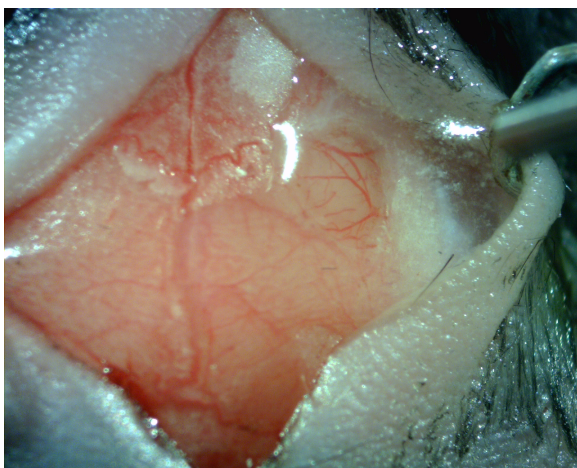
Figure 5: *Typical CCI preparation. Shaved sterilized skin is retracted, 2mm craniotomy is seen to the right of top center, under a saline meniscus. Impactor tip is to the right of the craniotomy. We have performed this CCI procedure in >75 animals so far.*

STAT3 conditional knockout (STAT3-CKO) enhance our mechanistic understanding of TBI effects. Our collaborator Dr. Michael Sofroniew was originally going to provide us with mGFAP-YFP mice, which express yellow fluorescent protein in astrocytes, allowing for specific imaging. These mice have unfortunately been inconsistent in their gene expression. As an alternative Dr. Sofroniew provided us with STAT3-CKO mice. These animals also allow for identification of astrocytes, but have the additional benefit that they allow testing of a signal pathway involved in astrocyte reactivity after TBI. STAT3-CKO mice have selective inactivation of STAT3 in astrocytes through the mGFAP promoter and show disrupted glial scarring and attenuated astrogliosis surrounding spinal cord injury [7]. STAT3 is ubiquitous member of the Jak-STAT signaling family, responsible for the signaling of many cytokines and growth factors [8]. STAT3 is expressed by most cell types in the CNS, and is up-regulated following traumatic brain injury in rodents [9]. The time course of phosphorlyated-STAT3 (activated STAT3) was shown to begin shortly after TBI gaining peak levels around 24 hours, and levels returning to baseline at 7-days, with phosphorylated-STAT3 shown to colocalize predominantly with astrocytes [9]. We are beginning to determine the consequences of selectively ablating STAT3 signaling in astrocytes in relation to TBI and cortical excitability, while simultaneously observing the response in the normal astrocytes of wild-type littermates. This tool significantly amplifies the mechanistic power of our proposal. However the cost of additional animals or experiments (specifically those involving STAT3 transgenic animals; wild-type animal experiments are as we proposed initially) has not and will not be borne by CDMRP as STAT3 mice were not in the original proposal.

Thresholding for seizure and spreading depression after CCI. CSD susceptibility was measured 48 hours and 7 days following injury. The CSD susceptibility procedure consists of re-opening the now fully healed suture in the anesthetized animal to expose the top of the skull. Carefully placed burr holes (being very cautious not to disrupt the dura matter) are placed in both the injured (ipsilateral) and uninjured (contralateral) hemispheres. Microcapillary tips are placed inside the burr holes producing a constant flow (~3.2 ul/min) of 0.9% saline to start. The animal's vital signs and temperature are monitored throughout the surgery. A thin layer of silicone oil is applied to the top of the skull to enhance visibility through the skull. Approximately 15 minutes of images taken with a CCD camera using 535 nm LED illumination (a wavelength that increases hemoglobin contrast) are acquired before the solution perfusing the burrhole is switched to 1 M KCl to induce CSD events. **Figure 6** displays the preparation. Difference images highlight the reflectance changes associated with CSD. Regions of interest placed in both hemispheres show the OIS fluctuations from each event, example shown in traces of **Figure 6**. The number of CSD events in both injured and uninjured hemispheres is recorded for approximately 1 hr following the first CSD event. **Figure 7** shows the

results thus far. Interestingly, we see no significant difference in CSD number, ipsilateral or contralateral to CCI, in sham vs. CCI treated animals or in STAT3 transgenic animals vs. controls, at 48 hours and 7 days after CCI. There is however a difference in the phenotype of the elicited CSDs in CCI cortex (not shown): likely because of the dead tissue in the CCI region, there is a significant increase in the number of circling CSD waves. The physiological significance of this finding is as yet unclear; we are developing tools to better analyze these complex datasets.
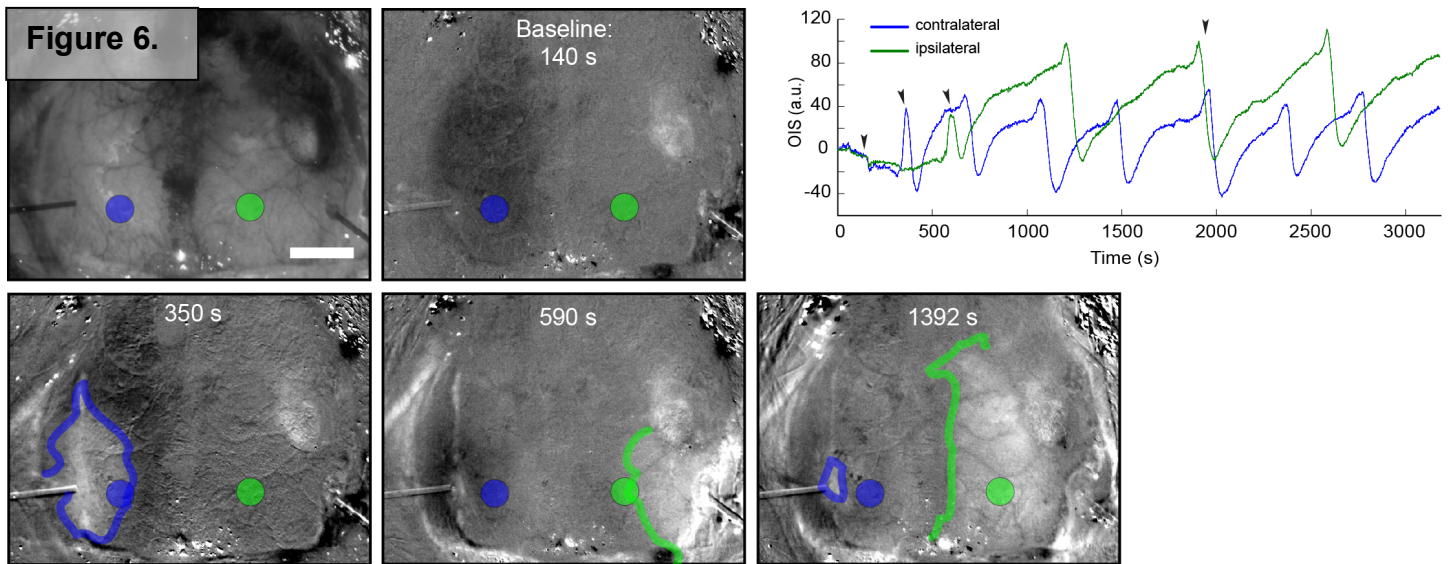
Figure 6.

Figure 7.
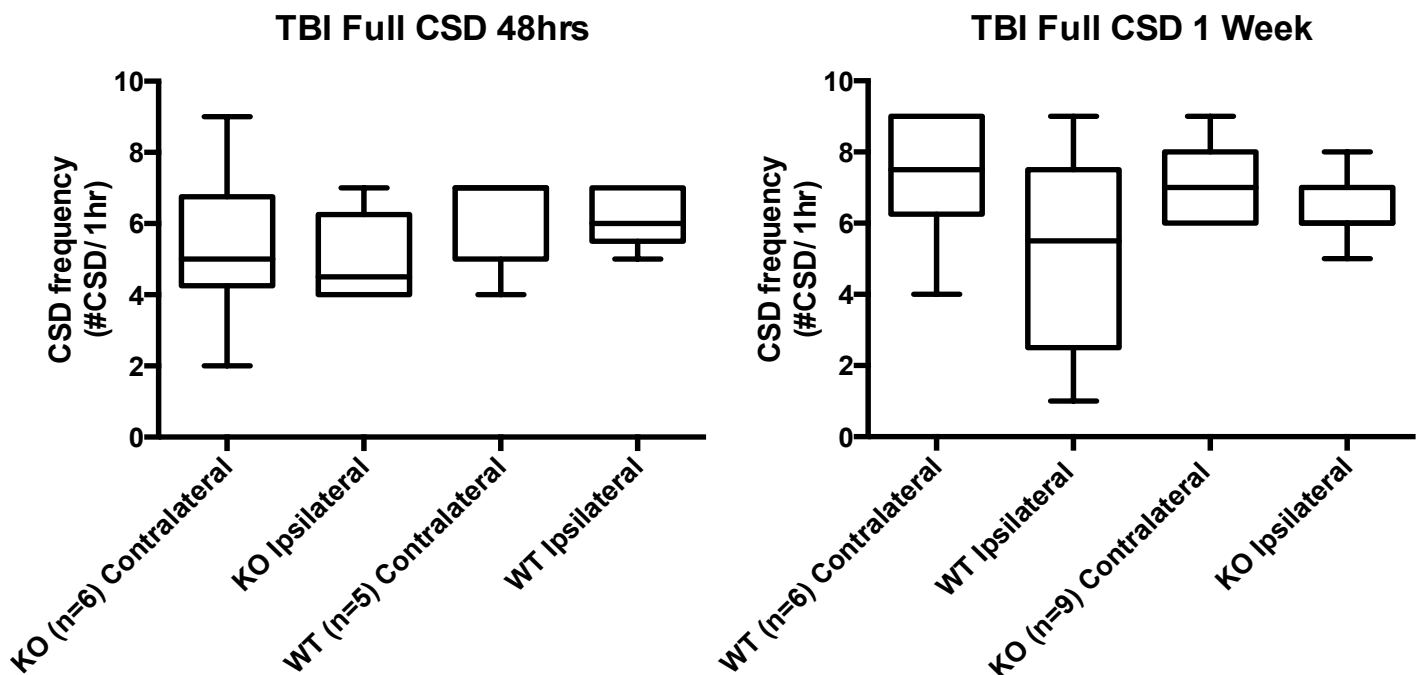
Subtask 3. Perform two-photon experiments 72 hours after CCI.

Cell-type-specific labeling and subcellular resolution imaging after TBI.

To uncover the cellular processes involved in TBI, we have developed all necessary two photon microscopy methods, in combination with *in vivo* whole-cell electrophysiology techniques (see below). Two-photon microscopy is used to accomplish longitudinal in vivo studies of anatomical changes and to study changes in calcium dynamics, perfusion, and metabolism. The use of transgenic animals with cell type specific fluorescence, like the GAD67 delta neo mouse, expressing green fluorescent

10

protein in interneurons, provides the chance to monitor cell-specific changes caused by the TBI experiment. In addition, the use of astrocytic specific dye (SR101) allows the simultaneous inspection of neuronal and astrocytic changes.

Visualization of astrocytes is important to the goals of the grant, and we have tried different techniques to load SR101. The first techniques consisted in loading the astrocytes by loading SR101 topically in the area of the cortex we wanted to visualize, following the methods described in Nimmerjahn et al 2004 [10]. Briefly, a 100µM solution of SR101 in aCSF was applied to a selected exposed area of the cortex. To have a better loading of the dye, the dura matter should be removed or at least perforated and the solution topically applied for 5 minutes and washed away with aCSF. The second technique consisted of tail vein injection of the dye as described in Appaix et al. 2012 [11]. In this case, 20mg/kg of SR101 in physiological solution is tail vein injected. Usually, after half an hour astrocytes are clearly identified. This technique has proven to be more reliable (**Figures 8,9**) and with the convenience of not having to further touch the area of the cortex to be imaged (which can artifactually induce astrocyte reactivity).
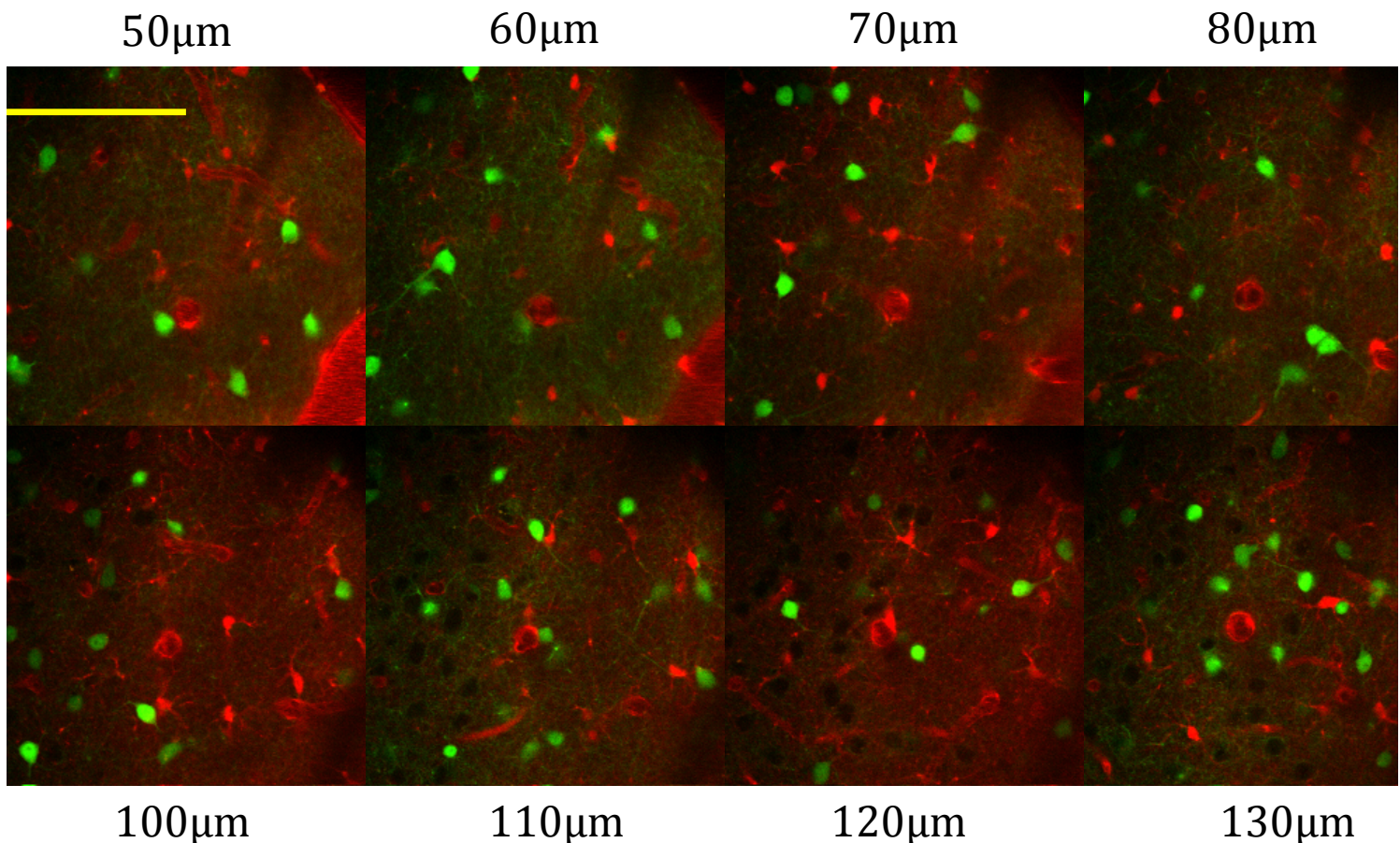
Figure 8: *Two-photon microscope imaging of a GAD67-Δneo mouse with all cortical interneurons identified with GFP and astrocytes stained with SR101. Interneurons are shown in green and astrocytes in red, compatible with fluorophore colors. Though pyramidal neurons are not fluorescent, they are identified by their darker appearance. The scale bar represents 100µm.*
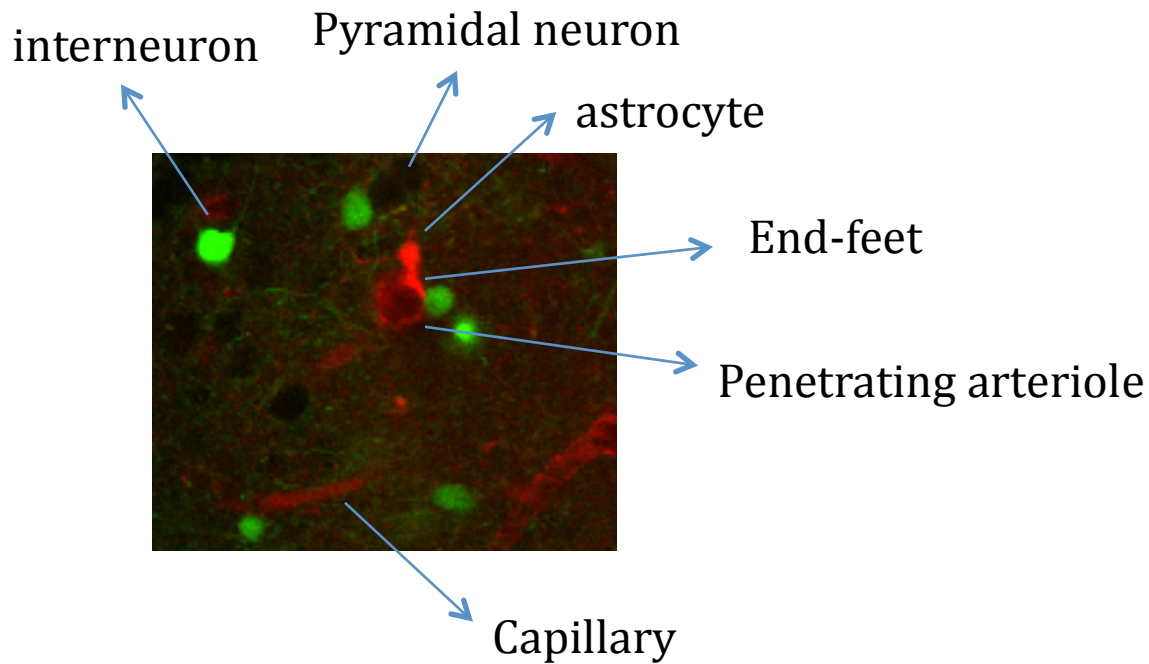
Figure 9: *All the anatomical elements of the network are identified: interneurons, pyramidal neurons, astrocytes and their end-feet, and the vascular components.*

Dendritic beading and cell swelling caused by cortical spreading depression (CSD), which accompanies TBI.

CSD is a massive depolarization that occurs during and after TBI. It causes significant structural and functional changes, including (**Figure 10**) dendritic beading and cellular swelling similar to what is seen during ischemia (except that it appears to be reversible).
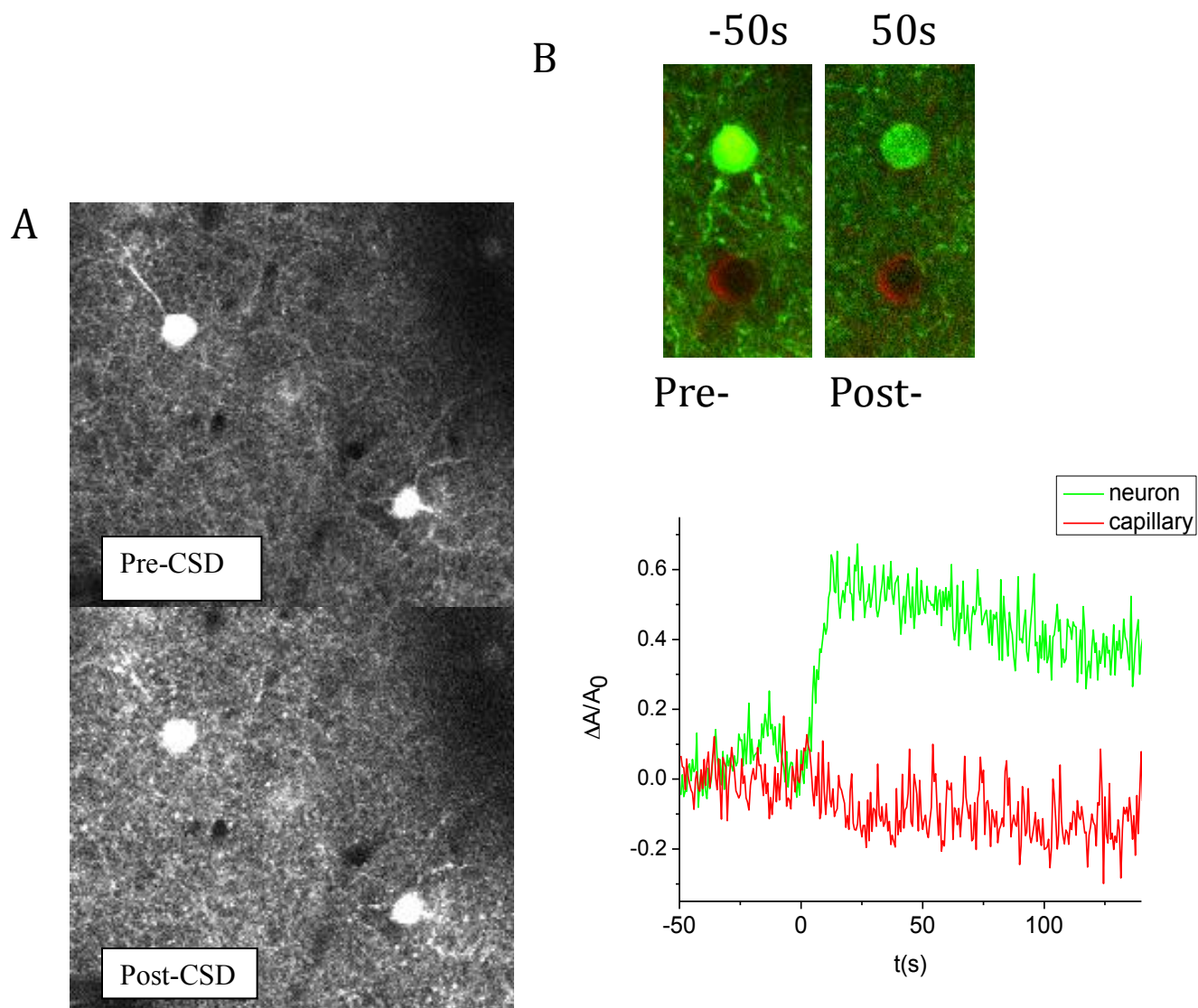
Figure 10: *A) Neuritic beading of the interneurons appears after a CSD event. The beading is visualized as small fluorescent dots in the neural processes. B) Cells swell after CSD. Time traces of the area of the neuron (shown in green) and of a capillary (red) are displayed. The area of the neuron increased more than 50%.*

Alterations in perfusion and metabolism after CSD.

We have implemented methods to monitor blood perfusion and metabolic condition of cortex by two-photon microscopy. By injecting FITC-dextran dyes into the blood a real time quantification of the perfusion is accomplished (**Figure 11a,c**). Detailed imaging of the vessel wall can be obtained with Alexafluor633, which labels elastin filaments (**Figure 11b**). Finally, the intrinsic fluorescence of the cortex can be monitored providing information about the NAD/NADH ratio and thus the tissue metabolism which is ultimately governed by perfusion (**Figure 12**). We have successfully used these techniques to describe changes caused by CSD and are progressively implementing them after CCI (a priority is neuronal recordings and these were done first – see below).

13
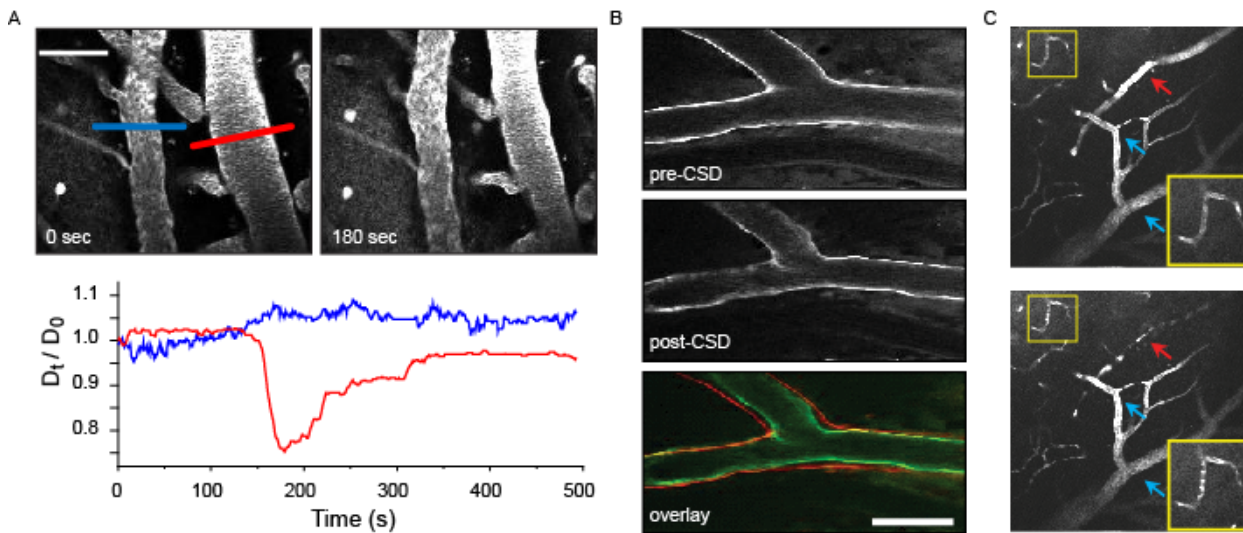
Figure 11: *Massive vascular changes during and after CSD. A. Two photon images of a cortical artery and vein are shown before and during a CSD. Diameter changes were calculated across their cross-section (artery: red, vein: blue) and displayed as time traces in the plot below (scale bar, 50 μm). B. Arteries also undergo morphological changes (labeling of elastin fibers with AlexaFluor 633), becoming more irregular (scale bar, 50 μm). C. Intracortical vascular dynamics during CSD. Images from 50 μm below the cortical surface show penetrating arteriole (red arrow), draining veins (blue arrows) and capillary (yellow inset). Plasma is labeled with 70 kD fluorescein dextran. At baseline, blood flow blurs individual red blood cells (RBCs). During CSD, arteriole (but not vein) constricts massively. Capillary blood flow stops, revealing individual RBCs as dark spots. Shortly after CSD passage, arteriole dilates beyond baseline, but capillary flow is still compromised. Scale: arrows are 50 μm long.*
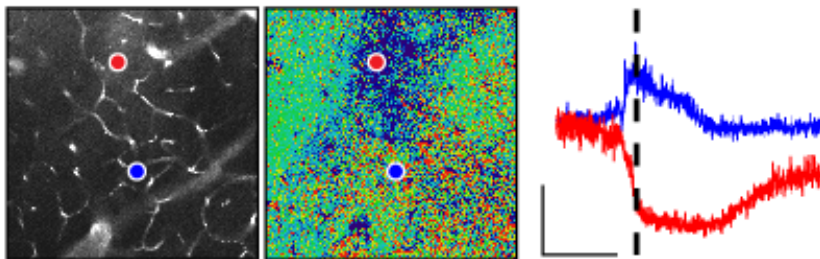
Figure 12: *Fluorescein dextran labeled capillaries 250 μm below the cortical surface (left). NADH intrinsic fluorescence image from same location (center), during peak CSD-associated changes (dashed line on graph). NADH oxidation (red; darkening) and reduction (blue; brightening) can occur, depending on location, however most regions show reduction, consistent with the metabolic challenge of CSD. Calibration: 10% change from baseline; 45 seconds.*

Calcium imaging with Oregon green BAPTA1-AM.

We have implemented calcium imaging of cortical cell populations by bolus loading of Oregon green BAPTA1-AM (OGB). Oregon-Green 488 BAPTA-1 AM is prepared at a concentration of 1 mM. We use a 20% solution of Pluronic F-127 in DMSO and we dissolve 50μg of OGB in it to a concentration of 10 mM. Then this solution is further diluted (to a 1mM solution) in a HEPES aCSF (150mM NaCl, 2.5mM KCl, 10mM Hepes, with a pH of 7.4). The calcium indicator is loaded in a glass pipette and bolus loaded in the cortex at a depth of 200μm (typically using a pressure of 10 PSI for 1 minute) [12]. Imaging is started after an hour of the pressure injections. An example of calcium imaging during CSD event is shown in **Figure 13**. However while is has been useful in uninjured animals, OGB use after TBI has proved problematic; thus we have switched to genetically encoded calcium indicators.

14
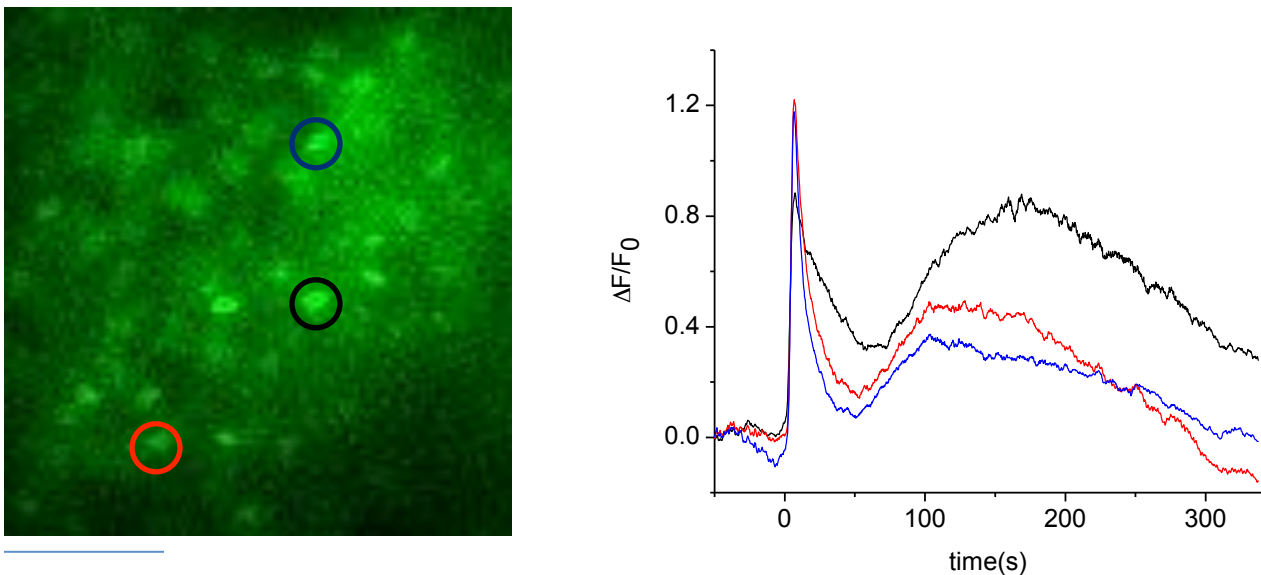
Figure 13. OGB1 AM loading of a cell population in layer 2/3 of somatosensory cortex (OGB1 selectively labels neurons, but some astrocyte fluorescence is also possible). The fluorescence changes corresponding to the occurrence to a CSD at t=0s in the areas depicted by colored circles are shown in the plot in the right side. The bar indicates 50 µm.

Imaging with genetically encoded calcium indicators (GECI).

The alternative to dye loading is to use GECI [13,14]. We now routinely use GCaMP5 or 6 delivered by viral vector injections. The use of AAV2/1.hSynap.GCaMP5G(GCaMP3-T302L.R303P.D380Y).WPRE.SV40 reveals neuronal specific population calcium activity in the relevant area of the cortex, because the expression is driven by the neuron-specific Synapsin promoter (**Figure 14**). For this procedure, the animal is anesthetized with isoflurane (5% for induction and 1.5% for the rest of the procedure) and put in the stereotactic apparatus for the correct identification of the region of interest. A small craniotomy is performed, and a small volume (~1 µL) of the virus suspension is loaded in a glass pipette and pressure injected. The craniotomy is sealed with silicone elastomer and the skin reapposed with vetbond. The animal is administered with antibiotics and analgesics and recovered for 2 or 3 weeks to allow for a sufficient expression of GCaMP. After this the animal is prepared for imaging.
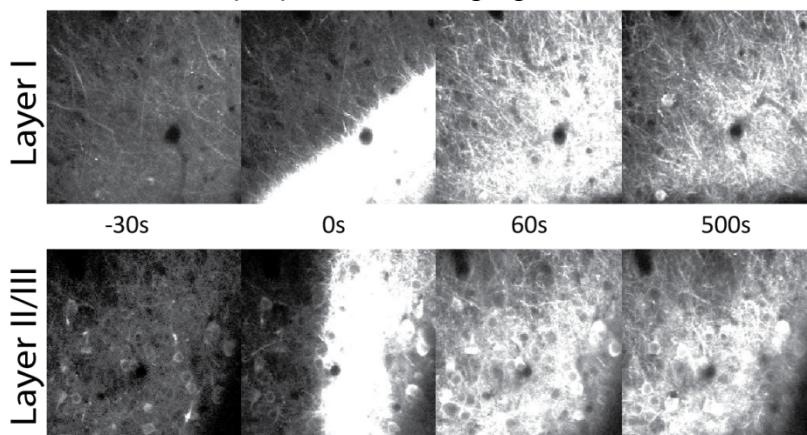
Figure 14: Layer specific calcium transients in neurons loaded with genetically encoded calcium indicator. An adeno-associated virus encoding GCaMP5 under the synapsin-1 promoter (neuronal specific) was injected in the cortex and 3 weeks later the mouse was prepared for imaging (craniotomy over somatosensory cortex). The same area was imaged at two different depths, corresponding to layer I and layer II/III. Sequences of images show the propagation of the CSD in these two different depths.
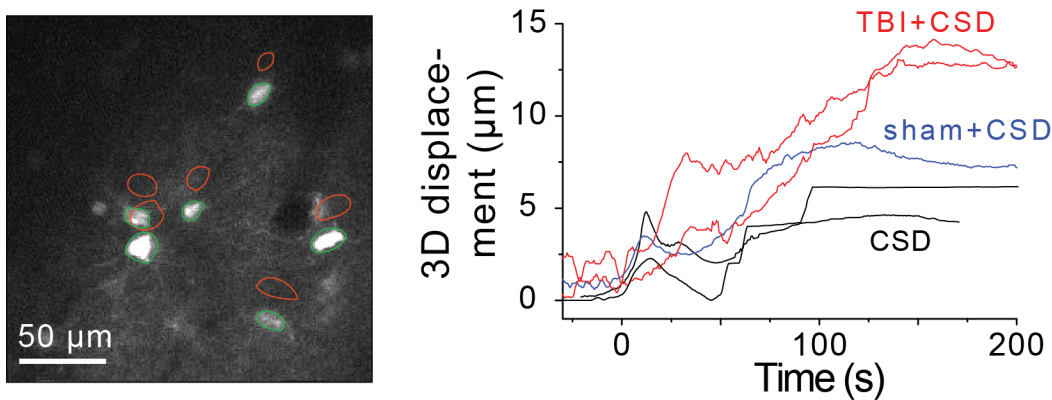
Figure 15. *TBI increases mechanical displacement caused by CSD. Two-photon image (left) shows displacement of GFP labeled interneurons (layer 2/3) in the scanning plane for an animal 48 h after CCI TBI. CSD was induced by topical application of KCl. Red: pre-CSD position; Green: post-CSD position. Plot shows Euclidean distance calculated by a correlation-based algorithm for different animals. Red: mice with TBI 48 h before experimentally induced CSD; Blue: Sham TBI 48 h prior to CSD. Black: Mice with no TBI procedure.*

### Neuronal two-photon imaging after TBI.

Two photon imaging after TBI has been technically challenging but ultimately successful. We initially used Oregon Green BAPTA multicell bolus loading, where an organic dye is injected acutely during the experiment 72 hours after CCI. Loading (2 animals) was much worse than in non-TBI animals, with very poor signal. This prompted the use of virus-delivered genetically-encoded calcium indicators. The indicator is injected 2 weeks before CCI in a burrhole 2-3 mm anteromedial to the CCI craniotomy, CCI is delivered, and animals are imaged 72 hours after CCI in a craniotomy between the burrhole and the CCI craniotomy. Of 17 experiments so far with AAV-delivered GCaMP5 as the indicator, 9 have been successful, in that there is good functional signal-to-noise, proper cytoplasmic but not nuclear loading of the dye (see **Figure 14**), and excellent delineation of anatomy. The majority of the 8 unsuccessful experiments were initial trials; success rate has improved with time. And many of the 'unsuccessful' experiments still yield useful data – e.g. good calcium signal but relatively poorer anatomical resolution. **Figure 15** shows increased tissue displacement associated with CSD in a post-TBI animal.

Investigation of migraine mutant mice in parallel with wild type mice after TBI.
Patients with migraine are more likely to develop post-traumatic headache after TBI[20]. Though this award did not proposed the use of migraine mice (no CDMRP funds are used for these mice), we are separately funded for this effort. We have conducted experiments on mutant and wild type mice together, as we believe this will provide deeper insight into the mechanisms of PTH in our service personnel, many of whom have migraine.

We use casein kinase 1 delta (CK1d) mutant mice[19] to compare with our wild type animals. A mutation in CK1d was identified in two families having sleep phase syndrome and typical migraine with aura. Mice genetically engineered to express this mutation showed a reduced threshold for CSD and an increased sensitivity to nitroglycerine induced mechanical and thermal hyperalgesia, both considered migraine relevant phenotypes[19]. Our hypothesis is that CK1d mice will have an amplified response to TBI compared to their wild type littermates.

We recorded calcium transients during CSD in WT and CK1d animals (5 in each group) 72 hours after sham or CCI (**Figure 16**). There were significant differences in all measures. The left figure panel shows calcium fluorescence maxima associated with CSD – these were significantly decreased after CCI in both groups – however in both sham and CCI animals, fluorescence maxima were significantly larger in CK1d animals. While fluorescence maxima were decreased after TBI, the duration of CSD associated calcium transients was significantly longer. The result is that the total calcium load (right panel; area under the curve of the calcium transient) was significantly greater after

CCI than sham; and once again the change was larger in CK1d animals than WT in both conditions. We interpret these findings as evidence of increased neuronal excitability after TBI, which is enhanced in animals carrying a migraine mutation. These results may help explain both the tendency toward headache and seizures after TBI, as well as the greater predisposition to PTH in patients with migraine.
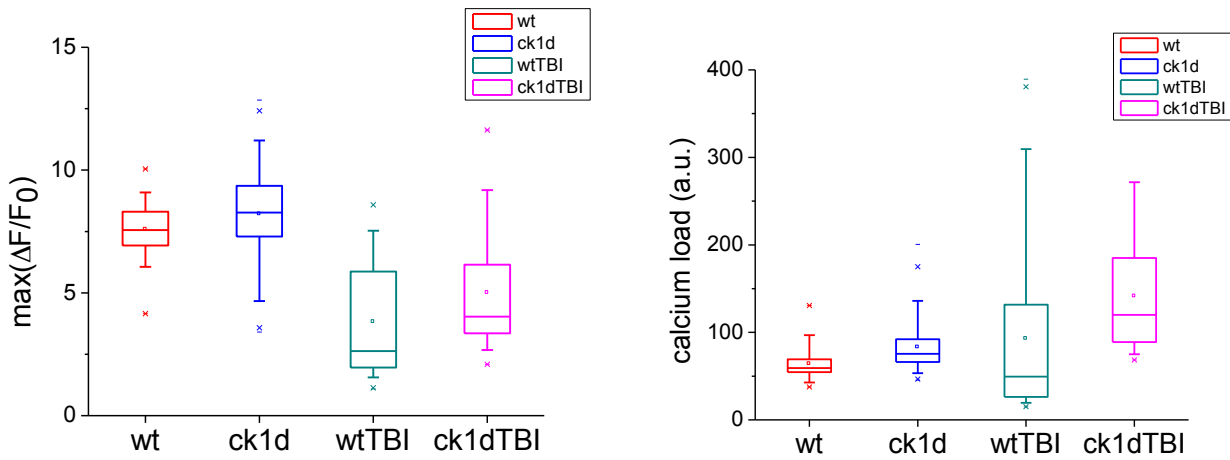
Figure 16

Astrocyte-specific calcium imaging.

We are interested in understanding the astrocytic changes related to TBI. The use of Fluo4-AM yields astrocytic specific calcium signal (a functional signal as opposed to SR101 which does not change with activity) that can be confirmed with SR-101 labeling [10,12,15]. We have successfully used this dye in WT and in STAT3-CKO animals. The dye loading method was based on the methods described by Hirase et al 2004 [15].
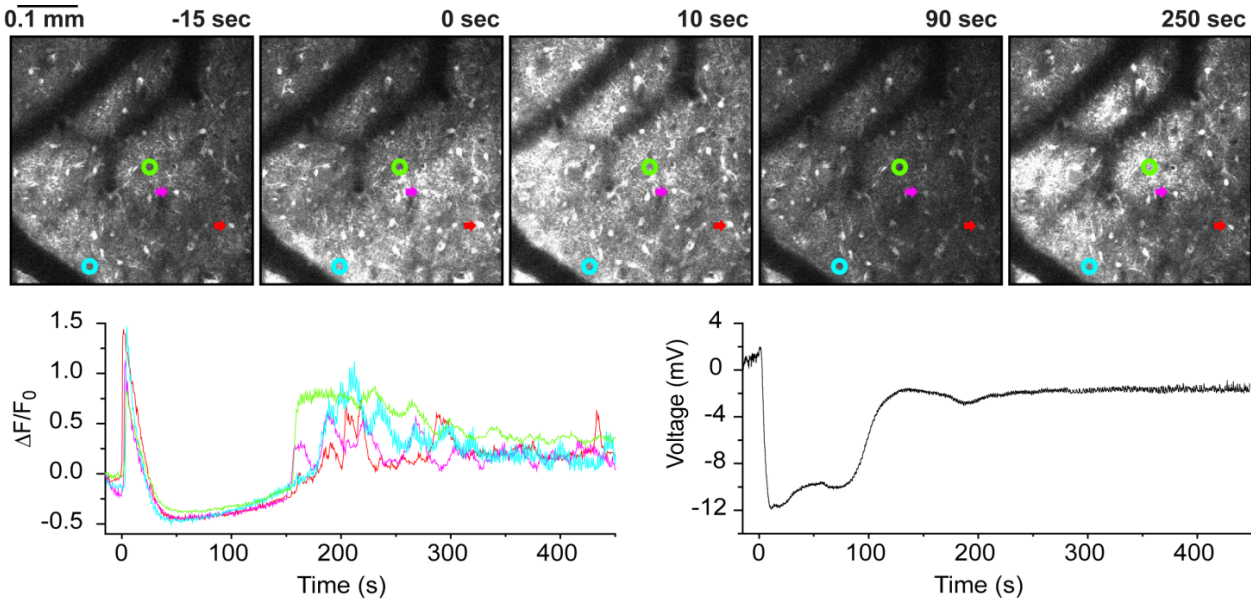
Figure 17: *Massive changes in astrocyte calcium activity during and after CSD. Fluo4-AM was used to load astrocytes in the somatosensory cortex of a WT mouse.* ***A.*** *Time sequence showing the propagation and aftermath of CSD. The wave propagates through the imaging window at 0 s. Colored arrows represent astrocytes and circles represent neuropil. Imaging depth 100 μm.* ***B.*** *Time traces of the fluorescent changes of the astrocytes and neuropil indicated in A. There is a massive increase in astrocyte calcium activity during the wave, followed by a decrease then a subsequent increase to*

17

beyond baseline. There is a persistent increase in rhythmic calcium activity. Right hand trace shows field potential deflection associated with CSD, and sustained depolarization after the wave (field potential does not return to baseline) which corresponds temporally with increased calcium activity.

In vivo *whole cell recording to determine the mechanisms of increased cortical excitability after TBI.*

To study functional changes in cortical neurons after traumatic brain injury, we have used *in vivo* whole cell electrophysiological recordings[16,17]. These recordings will be essential to directly demonstrate synaptic activity associated with sensory processing and behavior.

Surgical Preparation.

Mice (n = 50 to date) were anesthetized using intraperitoneal injection of urethane (1.2- 1.5 g/kg). Body temperature is controlled using a heating pad and maintained at 37°C throughout the experiment. A round craniotomy (approx. 2 mm in diameter) is made in the barrel cortex region (3-4 mm lateral to the midline and 1-2 mm posterior to the bregma). Dura is removed using a 30 gauge syringe needle and fine forceps. Durectomy with less bleeding has been an important step in order to have a clean passage for patch electrode through the tissue. Agar (1%) is placed on the brain surface to keep the surface moist.

Electrophysiological Recordings.

Intracellular recordings are performed using thick-wall glass pipettes pulled from borosilicate glass capillaries (OD 1.65 mm, ID 1.2 mm, Garner Glass, Claremont, CA) with a P-87 Flaming-Brown puller (Sutter Instruments, Novato, CA). Patch electrodes of 5-7 MΩ are used (tip size of 3-4 µm). A patch pipette is filled with intracellular solution containing (in mM; pH = 7.2): 120 K-gluconate, 1 NaCl, 5 EGTA, 10 HEPES, 1 $MgCl_2$, 130 CsCl, 1 $CaCl_2$, 2 ATP, 0.05 mM Alexa 594 (for visualized experiments). Signals are amplified using a Multiclamp 700B amplifier (Axon Instruments, Foster city, CA). Signals are sampled at 10 kHz and low-passed filtered at 2 kHz. Data are acquired and stored on a PC using a Digidata-1320A digitizer (Clampex, Molecular Device, Union City, CA), and pClamp 8.2 software (Clampex, Molecular Device, Union City, CA). Electrode is placed on the surface with positive pressure of 30 kPa and advanced to a depth of 100-200 µm. Once the electrode is lowered to the desired cortical depth (layer I-II), pressure is reduced to 4 kPa. In voltage clamp mode, the pipette is moved slowly in steps of 0.04 µm through the layers of the cortex while monitoring the current response to an applied voltage step (10 mV amplitude). We further lower the pipette until we observe a consistent reduction in response amplitude (approx. 50%), which indicates an increase in electrode resistance. Then positive pressure is removed to zero and suction is applied if necessary to get a gigaseal (a greater than giga-ohm series resistance recorded through the electrode). The command potential of -70 mV is applied. Negative pressure is applied to obtain a whole-cell configuration. Sometimes a gigaseal mode is left without perturbing, to perform cell-attached experiments. In the current-clamp mode, we record the spontaneous and evoked activity. Cortical spreading depression is induced by pin-prick and recorded (**Figure 18**).
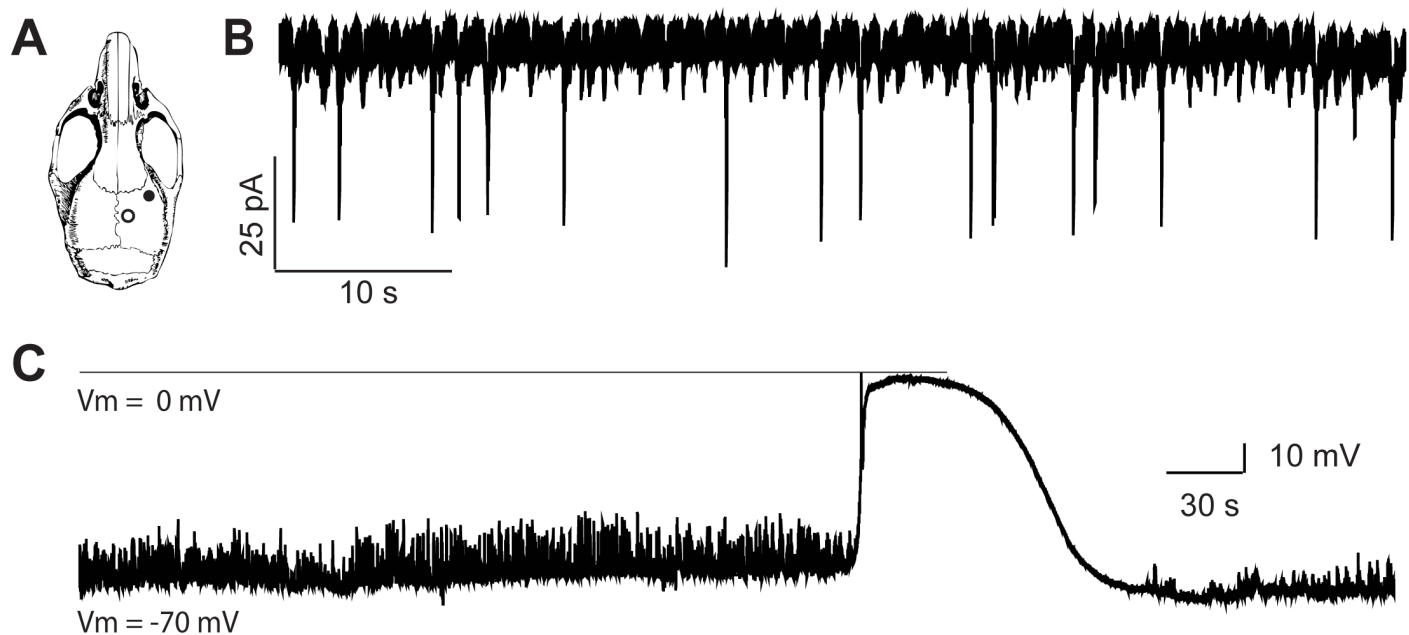
Figure 18: Whole-cell patch clamp recording of CSD in vivo. A. Schematic representation of the mouse skull demonstrating the location of craniotomy-durectomy for a single-cell recording. Closed and open circles represent locations for electrode placement and CSD induction, respectively. B. Membrane current traces showing spontaneous synaptic activity in layer II somatosensory neurons. C. Membrane potential changes during CSD, measured with patch pipettes filled with K+-gluconate. Following the induction of CSD with pinprick, the membrane potential reached 0mV during the peak of CSD. Note the reduction in neuronal firing after CSD..

In another set of experiments, we performed visualized whole-cell recordings using two-photon microscopy. Our approach is to use 'shadow patching' technique as described in the grant. Briefly, we eject the fluorescent dye Alexa 594 into the extracellular space. As described by Kitamura et al 2008 [18], individual neurons become visible as dark shadows against the bright fluorescence background. However, in our hands, we were unable to visualize neurons even under high power and different sets of ejection systems. At this stage, we are confident in our skills using blind patch techniques, as well as visualized patch recordings in either GFP or GECI-labelled cells to perform all the experiments outlined in the proposal.

The success rate for whole-cell recordings *in vivo* depends on many factors such as cortical movement, electrode positioning (angle of approach), and the craniotomy preparation. The stability of recordings is mainly associated with breathing and heartbeat-related movements of the animal. Another issue is to obtain seal resistance between the pipette and cell in a giga-ohm range. We were able to reduce cortical motion by preparing small craniotomies. Anesthetics are known to alter the breathing-associated movements so we tried using different compounds such as urethane or isoflurane or a mixture of both. Pure isoflurane results in poor seal quality, and pure urethane is difficult to control. In our hands, we obtain the fewest artifacts and best anesthetic control with a combination of urethane (0.25 mg/kg, supplemented as necessary) and isoflurane (0.2-0.8 %).

Spontaneous recordings of somatosensory cortical neurons. Whole cell recordings were made in the current clamp mode from neurons in layer 2/3 of mouse somatosensory cortex. Spontaneous post-synaptic potentials (PSPs) and "upstate events" (defined as spontaneous membrane depolarizations) were routinely observed under normal conditions (**Figure 19**). Neurons were classified as principal cells exhibiting regular spiking (RS) and intrinsically bursting (IB) phenotype, consistent with previously reported *in vivo* (Barrel cortex: Zhu and Connors 1999) and *in vitro* (Connors and Gutnick 1990) studies (**Figure 20**). These data are based on recordings from 23

neurons. Most of the neurons (65.2 % of neurons) exhibited regular spiking firing, i.e., cells fired a single AP to depolarizing current pulses and only two cells were suspected to be interneurons. Increasing the current intensity increased the firing frequency of RS cells and the firing frequency was always less than 100 Hz. Spontaneous recordings from those cells also exhibited single neuron AP but occasionally fired double action potentials (13.3% of cells). Half-width of AP's ranged from 1.92 to 2.96 ms, with a mean of 2.43 ± 0.14 ms. Some neurons responded to current with single or multiple bursts and they were classified as intrinsically bursting (IB) neurons (26.1 % of neurons). IB neurons have been defined *in vitro* (Connors *et al.*, 1982; McCormick *et al.*, 1985) and *in vivo* (Nuñez *et al.*, 1993). Increasing the current intensity changed the firing pattern to more RS-like firing without a burst. Bursts consisted of more than three action potentials, with firing frequency of IB cells' more than 100 Hz. IB cells fired doublet or triplet of AP's during spontaneous recordings, but occasionally fired single action potentials. Half-width of AP's for IB cells were 3.96 ± 0.33 ms. These characteristic patterns have been used previously to identify subpopulation of neurons (*in vivo,* Zhu and Conners, 1999; *in vitro* (Agmon and Connors 1989; Silva et al. 1991).
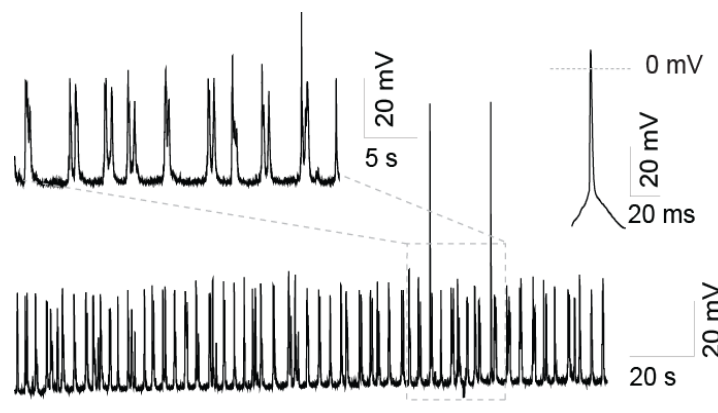
Figure 19. A representative trace of spontaneous activity recorded in the whole-cell configuration from layer 2/3 somatosensory cortex. Showing membrane potential traces from a layer 2/3 neuron in mouse somatosensory cortex displaying resting membrane potentials (down-state) and depolarized potentials (up-state). Boxed parts are shown in expanded time scales. Action potential is trimmed for clarity. Enlarged waveform showing the kinetics of an action potential.
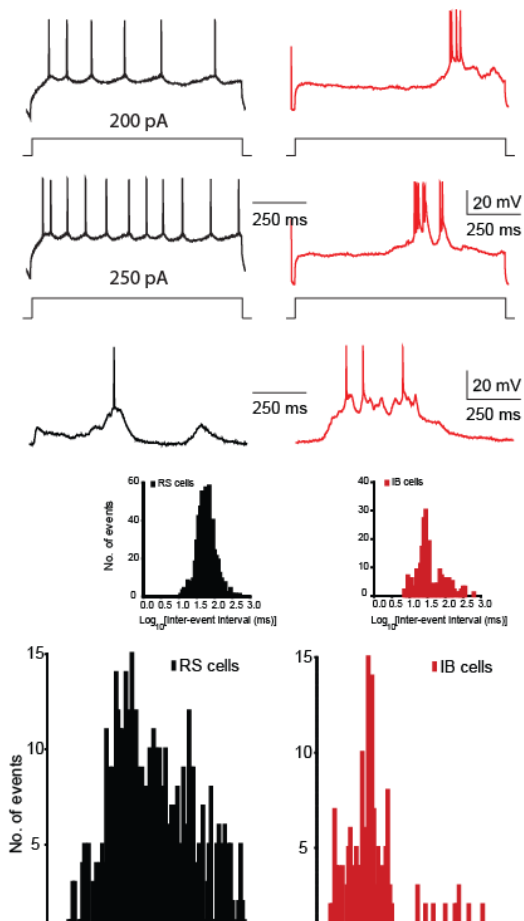

Figure 20: Spontaneous versus evoked responses of regular-spiking (RS) and intrinsically burst-spiking (IB) neurons. (A) Top and middle: Firing profile to depolarizing current pulses of two different current intensities. Bottom: voltage traces showing spontaneously occurring events. (B) Histogram for the log values of the interspike intervals in bursting and nonbursting neurons.

Our major efforts are now dedicated to recording after TBI (n = 50 so far). We collect data from wild-type and CK1d mutant animals (the latter are separately funded; no CDMRP funds are used for CK1d mice) on intrinsic membrane properties, synaptic input during and after sensory, chemical, and electrical stimulation, and cortical spreading depression, in areas near and distant from CCI TBI injury.

We now have datasets that are statistically powered to detect differences after TBI (**Figure 21**). Recordings are within 2 mm of the CCI lesion, or equivalently located by stereotaxic coordinates in sham animals.

Intrinsic membrane properties of wt and CK1d animals. To examine whether the injury was associated with a change in the intrinsic membrane excitability, we first examined the input-output curve by measuring the frequency of action potentials in response to a series of intracellular depolarizing current pulses. The number of action potentials was graded with the intensity of the depolarizing currents in pyramidal neurons. The slope of the input-output curve was not significantly changed in CCI animals, relative to sham (**Figure 21** A2,3). The rheobase was not altered in CCI neurons at 72 h post-injury, confirming no change in neuronal intrinsic excitability after injury. Other membrane properties including resting membrane potential, action potential threshold and input resistance, were similar in injured and sham cells (**Figure 21** A1).
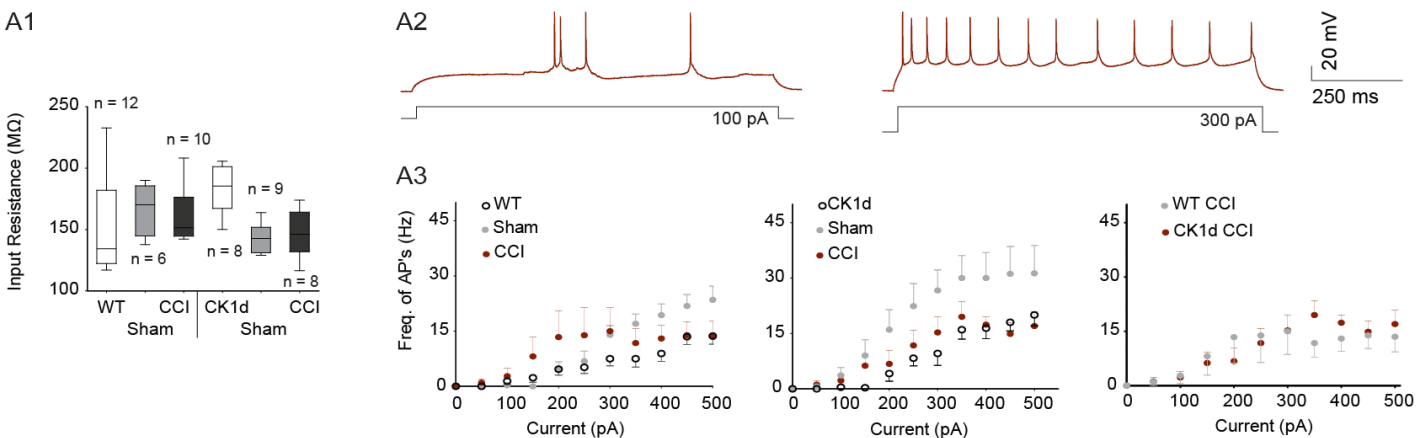
Figure 21. A1: Membrane properties such as resting membrane potential and input resistance were not changed after CCI in either WT or CK1d animals. A2: Whole-cell recordings from pyramidal neurons showing action potential firing at two different current injections. A3: Summary plots showing that the slope of input-output curve was not altered in any groups after CCI. Rheobase was not altered after CCI (data not shown).

Spontaneous activity in somatosensory cortical neurons. To assess the potential involvement of synaptic changes following brain trauma, we analyzed the properties of spontaneous synaptic neurotransmission in the layer 2/3 cortical neurons. Recordings from sham animals exhibited spontaneous post-synaptic potential (sPSP) amplitudes ranging from one to twenty millivolts. All neurons from CCI animals displayed sPSPs; however, the amplitude of their sPSPs was significantly smaller. Giant sPSPs (>10 mV) were mainly seen in sham animals, and were much less frequent in neurons from CCI mice. The histogram for log amplitude of the sPSPs in the wt CCI group was significantly shifted to the left, consistent with a reduced number of large-amplitude events ($p < 0.0001$; **Figure 22** A2). The histogram of log intervals of the sPSPs for wt CCI group was significantly shifted to the left, suggesting reduced interevent interval and thus increased frequency ($p < 0.0001$, **Figure 22** A1). Larger amplitude ($p < 0.01$; **Figure 23** A2) and longer duration ($p < 0.0001$; **Figure 23**

A3) but mildly lowered frequency (p < 0.01; Fig. 6A1) of post-synaptic potentials was observed in CK1d neurons after CCI.
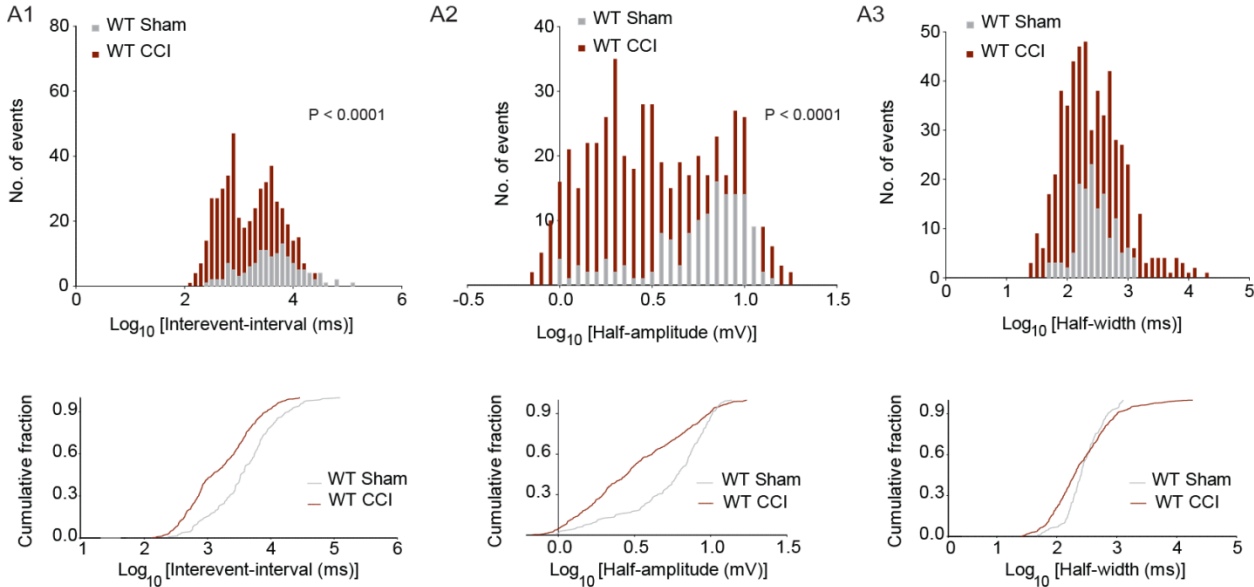
Figure 22. A1: Quantitative analysis of histogram for log interevent-interval of the post-synaptic potentials of neurons from WT animals showed leftward shift in the interval, indicating higher frequency events after CCI. A2: Histograms showing the distribution of amplitude of PSPs significantly shifted to the left, consistent with smaller amplitude events after CCI, relative to sham animals. A3: No significant changes in the duration of those events were observed after CCI in WT animals.
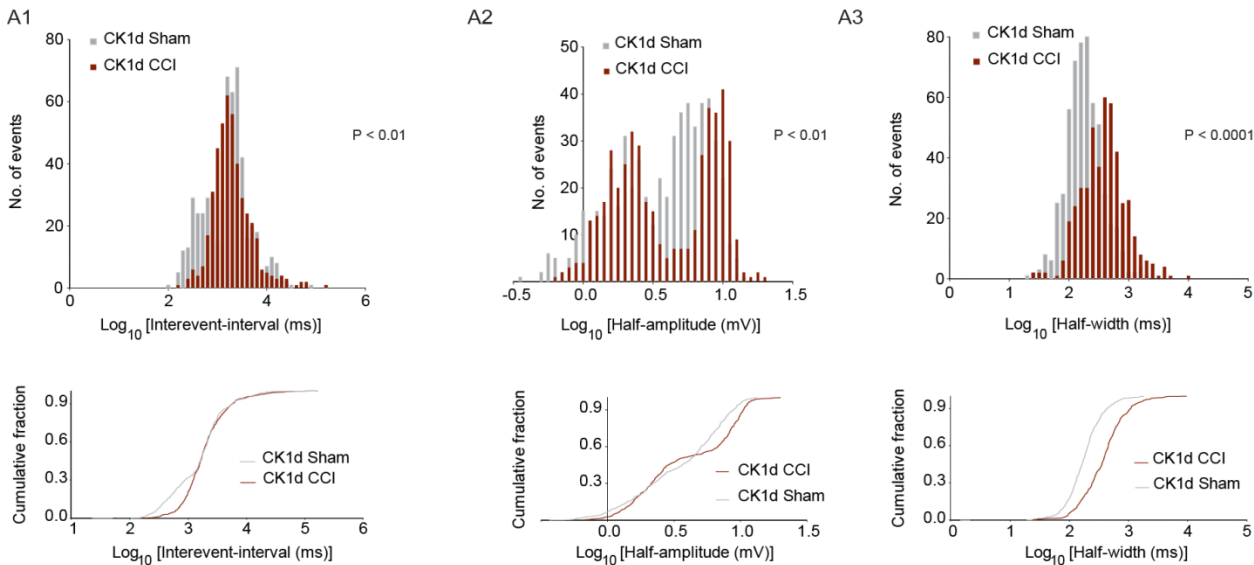
Figure 23. A1: Frequency distribution of post-synaptic potentials shifted to the right, showing reduced frequency of events from neurons of CK1d transgenic animals after CCI. A2,A3: Amplitude and duration of PSPs were significantly increased in transgenic animals after CCI, relative to CK1d sham animals. The corresponding histograms were shifted to the right in those group.

In striking contrast, CK1d CCI animals showed a significant *increase* in the duration (p < 0.0001; **Figure 24** A3) and amplitude (p < 0.0001; **Figure 24** A2) of sPSPs relative to wt CCI. These data suggest that principal neurons in layer 2/3 from CK1d mice contain more connections from local or remote structures and/or changes in the excitation/inhibition balance within the circuit. We are currently recording and analyzing inhibitory conductances that should delineate one of the mechanistic pathways underlying changes in the synaptic potentials.
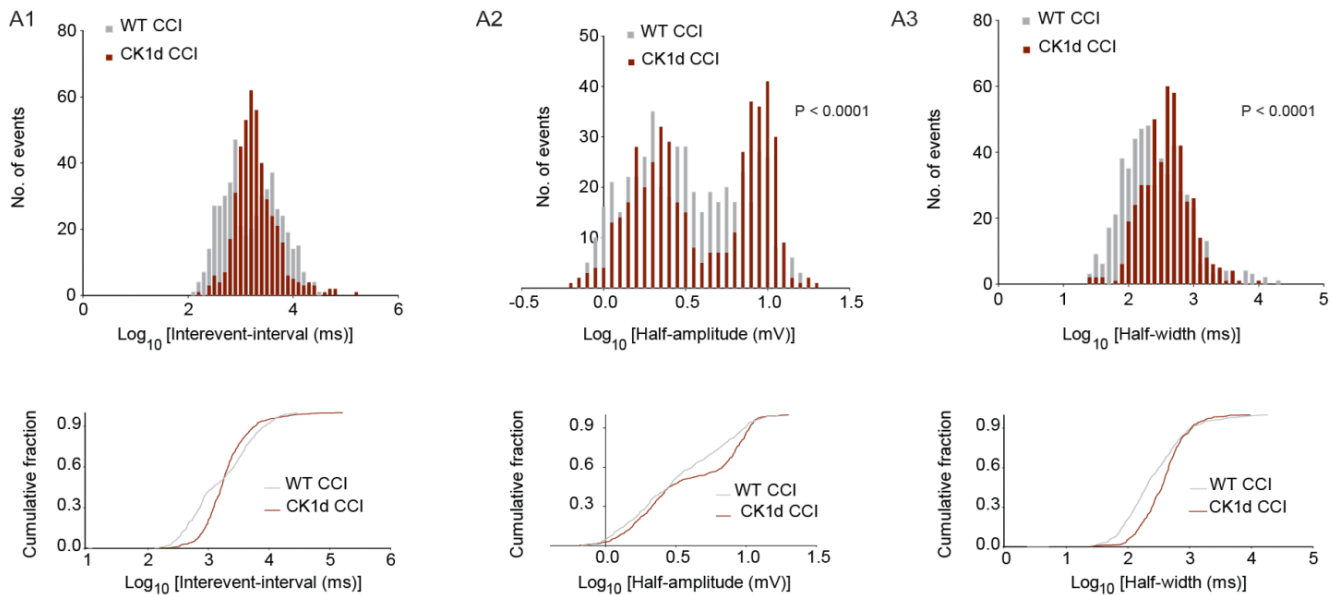
Figure 24. A1: No significant changes in the frequency histogram when comparing the two CCI groups - WT and CK1d. A2,A3: Histograms of amplitude and duration were shifted to the right, indicating larger amplitude and longer duration events in neurons from CK1d CCI animals, compared to WT CCI animals.

Summary

Our CCI data shows injury-induced increases in the frequency and decreases in the amplitude of sPSPs in layer 2/3 somatosensory neurons, 48 hrs post-injury, in WT animals. In contrast, larger amplitude and longer duration events were observed in CK1d mutants after CCI. These observations converge with our two-photon imaging data to suggest that traumatic brain injury leads to cortical hyperexcitability in both CK1d and WT (to some extent) animals at 48 hrs after injury, but that migraine genotype is additive to the excitability phenotype , congruent with the increased susceptibility to PTH in migraineurs. These results may help explain why PTH is more common in migraineurs.

Subtask 4. Perform two-photon experiments 72 hours after lipopolysaccharide injection, acutely after hypotonic ACSF perfusion.

Figure 25.

CSD number following 1M KCL
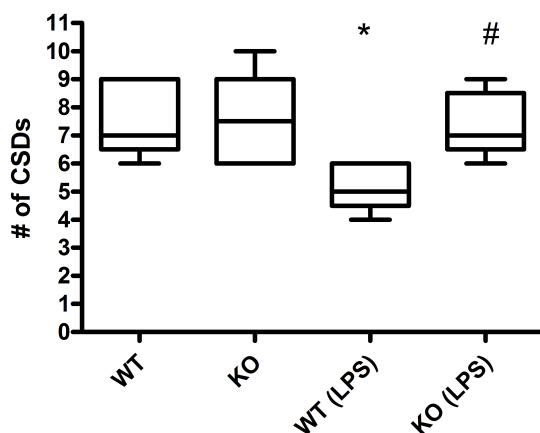
To ascertain the effect of a *low dose LPS injection* on cortical excitability, a group of 22 male animals was used to determine the effect of LPS exposure to CSD threshold. 6 WT and 6 KO animals were initially used to determine a baseline susceptibly of cortex to 1M KCl induced spreading depression. A subsequent group of 5 WT and 5 KO animals was injected with 0.5 mg/kg LPS i.p. The CSD susceptibility was measured 72 hours later. The CSD number following the first KCl induced event was recorded for 1 hour. The results are shown in Figure 5 (* = WT vs WT(LPS) $P < 0.05$; # = WT(LPS) vs. KO(LPS) $P<0.05$ One-way ANOVA Tukey's Multiple Comparison). LPS treatment reveals a GFAP cell expressing-STAT3 dependent reduction in CSD number in KO animals, an observation not seen in the untreated group (**Figure 25**). These data

23

show that *the immunological activation associated with TBI has effects on cortical excitability.* It appears that LPS-induced immunological activation reduces cortical excitability, in a manner that is dependent on astrocytic STAT3 signaling pathway function. These results are being supplemented with histology and 2-photon imaging.

To ascertain the effect on cortical excitability of *hypotonic ACSF perfusion*, 10 animals were implanted acutely with microdialysis probes (PlasticsOne, 13 kD membrane, 1mm length, 1mm depth into cortex) through a 2 mm craniotomy centered between bregma, lambda, sagittal suture, and temporal ridge. ACSF (in mM: 125 NaCl, 3 KCl, 1.25 NaH2PO4, 2 CaCl2, 1 MgCl2, 25 NaHCO3, 11 glucose, pH 7.4) was perfused at 0.1 ml/hr, either at full strength, half dilution with distilled water, 2/3 dilution with distilled water, or 100% distilled water perfusion. Reflectance signal was collected from regions of interest between 100 - 200 µm of microdialysis probe, or > 1mm distant from probe. Next, the same regions of interest were recorded during CSD. There was no significant difference in amplitude of either spontaneous or CSD-associated signal at any region of interest at any concentration of ACSF. Moreover, placement of microdialysis probes made analysis of signal closer to probe problematic. Finally, attempts at performing two-photon experiments with the microdialysis probe were unsuccessful because it was impossible to approximate the microscope objective to the tissue with the probe in place. We concluded that, due to the low yield of reflectance imaging and the impossibility of carrying out two-photon experiments even if reflectance imaging had been promising, that further microdialysis experiments should be deferred.

Subtask 5. Perform histological analysis on animals 24, 48, 72 hours, and 7 days after CCI TBI.

Histology using standard methods has been performed so far at the 48 hr and 7 days post injury time point. **Figure 26** shows the typical lesion pattern following our protocol. **Figure 27** shows Nissl stain at different magnifications including the CCI-lesioned region.
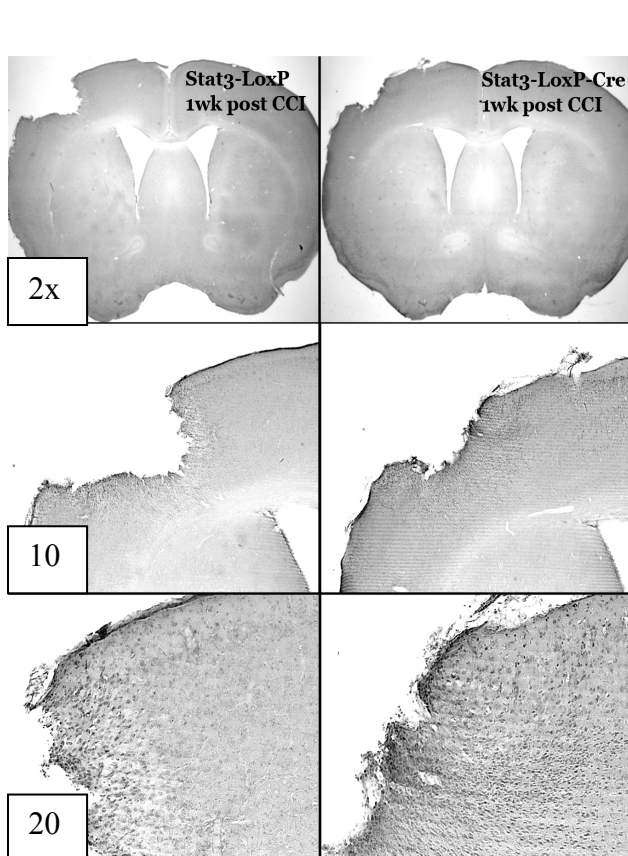
Figure 26: Typical brain after PBS and PFA perfusion, the CCI injury is approximately 2 mm in diameter.

Figure 27. Light microscopy images of Nissl stain displaying lesion area 1 week following impact in WT (Stat3-LoxP) and KO (Stat3-LoxP-Cre).

Our full repertoire of antibodies has been successfully tested and is now being routinely used after TBI. **Figure 28** shows neuronal (NeuN), microglial (Iba1), and astrocytic (GFAP) in tissue from the same anatomic location ipsilateral and contralateral to CCI. Neuronal numbers are not appreciably changed past the location of the glial scar. However there is a significant increase in astrocyte as well as microglial cell body and

24

process in the peri-contusion region but not the contralateral hemisphere, consistent with both astrocytic and microglial activation reported after TBI.
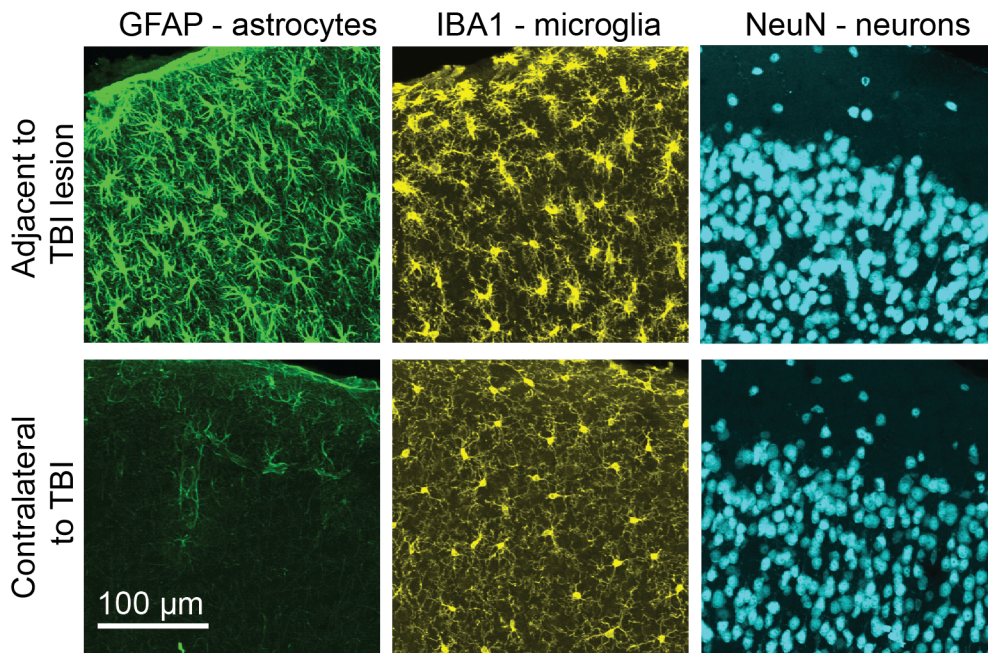
Figure 28: Tissue effects of TBI. A. Cortical sections of wild-type animals, 48 h after CCI TBI. Top images show cortex ipsilateral to the site of TBI, immediately adjacent to the lesion. Bottom images show contralateral cortex. There is an ipsilateral increase in GFAP staining and change in astrocyte morphology compared to contralateral cortex, suggestive of astrogliosis near the site of injury. Similarly, ipsilateral microglia (labeled with IBA1) appear to have a different morphology compared to those in the contralateral cortex. There is a mild increase in NeuN staining (labels neuronal nuclei) intensity ipsilaterally, but no clear change in morphology or number. Images shown are maximum intensity projections of approx. 20 optical sections through a single cortical slice.

Subtask 6. Perform plasma protein extravasation and brain water content experiments, analysis on animals 24, 48, 72 hours, 7 days after CCI TBI.

Pending. These experiments are a subset of our histological analysis, however they require separate processing. We have delayed these experiments and advanced the other histological techiques we use (see above) as the other techniques can be performed together.

Subtask 7. Analyze results, correlate with histological and other experimental data, prepare data for publication.

Analysis shown for each task in context.

Determine whether the chronic post-TBI state is marked by cortical excitability and behavior consistent with migraine and epilepsy

Major Task 2. Chronic experiments after CCI TBI (Brennan, Dudek, Months 1-48).

Subtask 1. Perform CCI, implant monitoring device, and monitor for chronic effects of TBI.

Ongoing. So far 29 mice (15 CCI and 14 sham controls) have undergone *continuous* monitoring out to 3 months after CCI. This is a major improvement over our originally proposed protocol, which would have had monitoring only in a 2-week window at the 3-month time point. Continuous monitoring offers the best chance of understanding the evolution of brain excitability changes after TBI, but the more difficult analysis of continuous-monitoring data does lead to slower throughput. Nonetheless, thus far, we have manually analyzed 30 of the 90 days of video-EEG recordings. Based on the first 30 days, we recorded spontaneous recurrent seizures (i.e., >10 days post-CCI) in 20% (3/15) of the mice (Fig. XX). In 40% (6/15) of the mice, we have identified "epileptic activity" in the electrographic data that has not yet been video-confirmed to be seizures, but appear promising. Given the labor-intensive manner of manual analysis of the video-EEG data, we are developing a semi-automated seizure detection program. We are optimistic that we can complete the experiments, but if need arises, we can revert to the original protocol. Animals tested with either protocol will be comparable as their housing/recording conditions will have been identical.
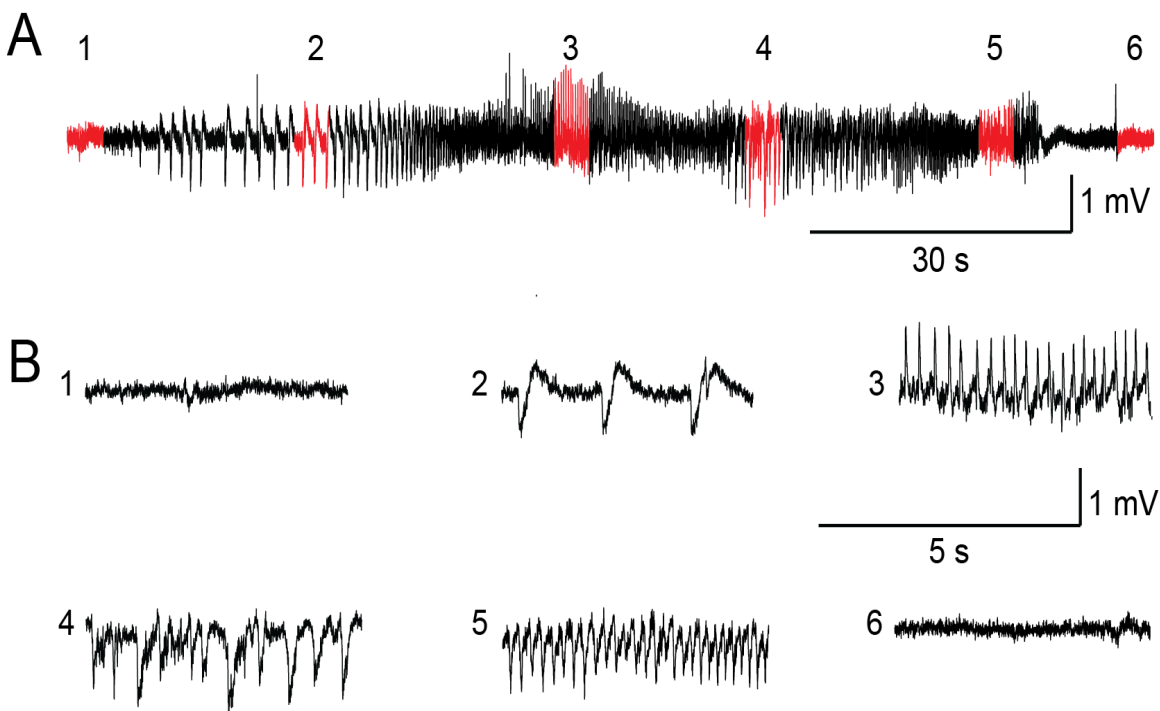
Figure 29 . A spontaneous recurrent seizure in a CCI-injured mouse 28 days after the injury. The lower traces are temporal expansions from the upper trace.

Subtask 2. Perform voltage sensitive dye experiments 3 months after CCI.

Ongoing. We have performed 3 preliminary experiments so far to optimize VSDI acquisition in our new lab location.

Subtask 3. Perform CCI, two-photon experiments 3 months after CCI.

Pending completion of acute two-photon experiments above.

Subtask 4. Perform histological analysis on animals 3 months after CCI TBI.

Ongoing for all animals above.

### Subtask 5. Perform plasma protein extravasation and brain water content experiments, analysis on animals 3 months after CCI TBI.

Pending. Will be performed simultaneous with task 1.f. above.

Subtask 6. Perform nociception behavior experiments (mechanical and thermal thresholds, rotarod) on animals 3 months after CCI TBI.

We have experience with both mechanical and thermal hyperalgesia testing; we realized that to have the clearest picture of headache relevant behavior (and potential confounds) after TBI, we needed to nest hyperalgesia testing in a more comprehensive behavioral phenotyping regimen. This regimen consists of open field testing to test for locomotor behavior, anxiety, and spontaneous behavior in general; then elevated plus maze testing to examine anxiety and also possible photophobic behavior; followed by testing of mechanical hyperalgesia after nitroglycerin, at 72 hour and 3 month time points. A particular reason to test more broadly is that stress (which is likely after TBI in both animals and humans) is associated with pain behavior and could confound results if not measured specifically. Our combined general behavior/stress/pain metrics allows us to correlate the measures and gain a more nuanced picture of the overall response. After the behavioral regimen all animals also undergo CSD testing to evaluate whether PTH-relevant cortical excitability is altered.

Figure 30 shows preliminary results of open field testing from CK1d and WT animals (L and R panels, respectively) before and 72h after TBI (7 animals per group of CK1d; 4 animals per group of WT). Thus far, CK1d and WT animals appear to have opposite post-TBI phenotypes: CK1d animals show a trend toward increased activity while WT littermates show a significant decrease. Stress behavior is typically associated with a decrease in activity in the open field center and more thigmotaxis (movement close to the walls). Thus WT animals show a potentially expected result after TBI. The CK1d response is more difficult to explain. It is possible that the animals are showing a 'reverse' stress phenotype after CCI; however it is also possible that the increased locomotion does not have to do with stress but a more generalized increase in sensorimotor activation. Increasing n for these experiments, combined with completion of elevated plus maze testing (not shown) which is more specific for stress/anxiety should help clarify the picture.
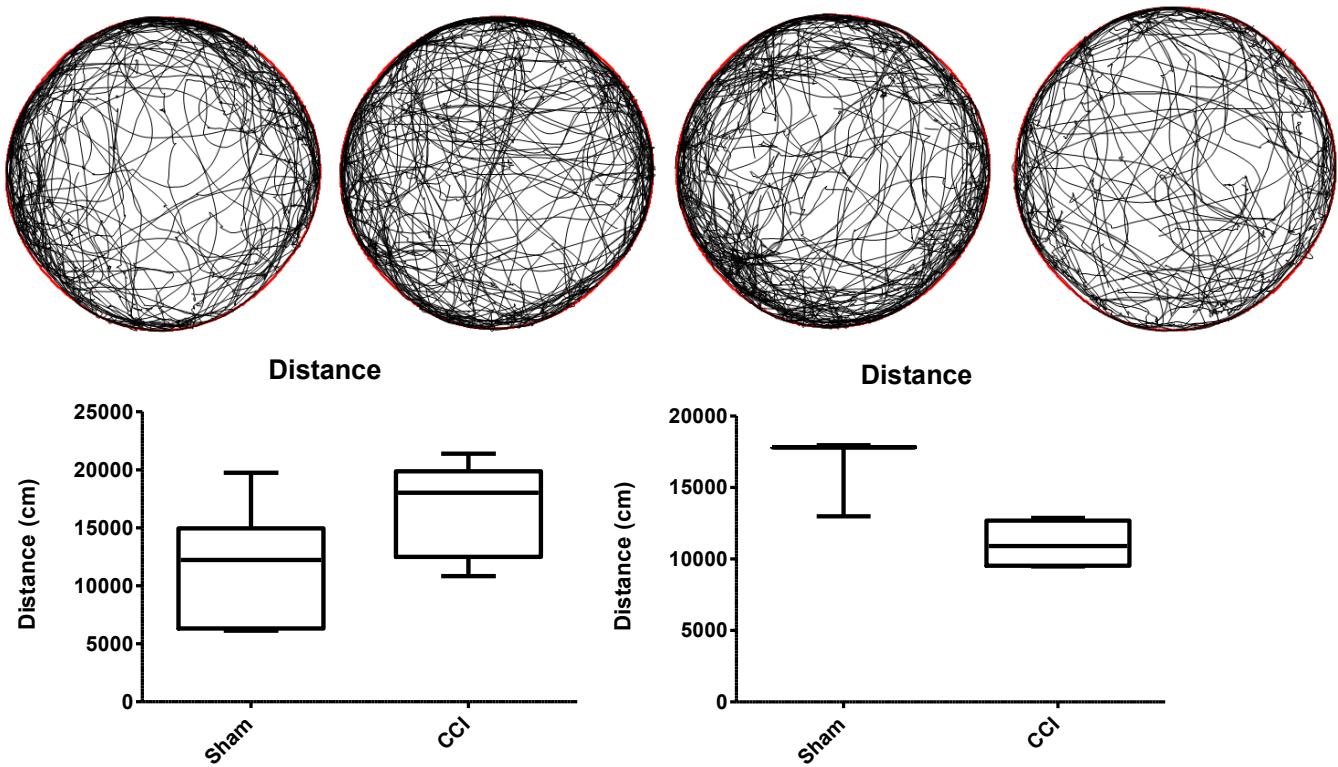
Figure 30

Hyperalgesia testing after NTG is ongoing; currently n is to small to draw conclusions.

Preliminary CSD testing is available for CK1d animals (n=4 per group). We observe a trend toward an increased number of CSDs 3 months after TBI, compared to sham treatment (**Figure 31**).
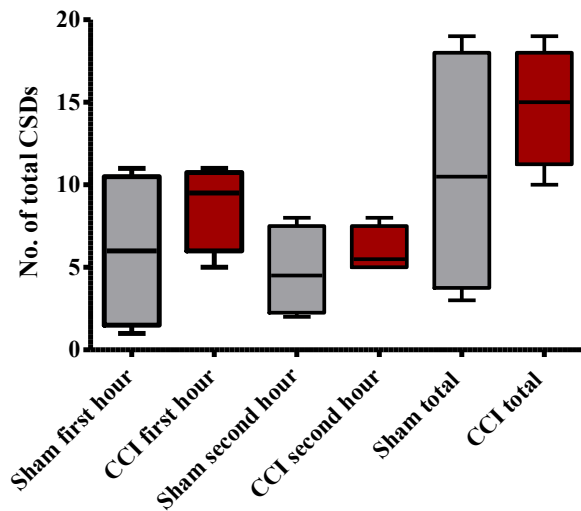
Figure 31

Subtask 7. Analyze results, correlate with histological and other experimental data, prepare data for publication.

Ongoing for each sub-task as task nears completion.

Specific Aim 3:
Test whether medications that modulate post-TBI plasticity reduce markers of epilepsy and migraine after TBI.

Major Task 3:
Chronic experiments after CCI TBI (Brennan, Dudek Months 1-48).

Subtask 1. Perform CCI, implant monitoring device, and monitor for effects of memantine treatment after TBI (3 months after injury).

Pending completion of Major Task 2 Subtask 1 above.

Subtask 2. Perform nociception behavior experiments (mechanical and thermal thresholds, rotarod) on animals 3 months after CCI TBI and treatment with memantine or placebo.

Pending completion of Major Task 2 Subtask 6 above.

Subtask 3. Analyze results, correlate with histological and other experimental data, prepare data for publication.

Ongoing for each sub-task as task nears completion.

KEY RESEARCH ACCOMPLISHMENTS

•Optimized controlled cortical impact TBI (CCI) parameters for mouse.

•Optimized EEG monitoring of mice after CCI to monitor for seizures and cortical spreading depression (CSD), continuously out to 90 days after CCI.

•Implemented two-photon microscopy and whole cell recording *in vivo* after CCI; reportable outcomes.

•Measuring susceptibility to CSD after CCI; reportable outcomes.

•Measuring post-traumatic headache-relevant pain metrics after TBI.

•Optimization and implementation of all histological techniques.

REPORTABLE OUTCOMES

•Memantine improves sensorimotor outcome after cortical injury – critical preliminary data for this proposal, proof of concept for our use of memantine; now published in *Stroke.*

•Lipopolysaccharide (LPS) treatment, used to model inflammatory effects of TBI, reduces susceptibility to CSD, but not in mice where astrocyte STAT3 signaling disrupted. To be supplemented by histology and 2-photon imaging.

•Altered sensory cortex pyramidal cell excitability phenotype after TBI in two-photon and in vivo whole cell recordings. Amplified phenotype in migraine mutant animals. Manuscript in preparation.

CONCLUSION

In the thirty months since the funding of this award we have established and validated all the experimental techniques, and completed most datasets. We are now completing the remaining datasets, analyzing data, and preparing for publication. We have also successfully extended our present work in order to maximize military-relevant synergies: we obtained a second CDMRP award extending the present research; in doing so we continue to develop a collaboration with a University of Utah engineer (Dr. Kenneth Monson) performing blast TBI. Blast TBI is not part of this grant but enhances our ability to model all effects of military TBI. In addition, we continue to work with our Brain Injury Network involving all TBI investigators at the University of Utah and the Wahlen VA. The goal of this group is to obtain a DOD or VA program grant application incorporating human and animal research.

So what?
If successful our work will:
•Define the natural history of excitable events in the brain after TBI.
•Determine the mechanisms of these excitable events.
•Develop treatments that prevent the progression to migraine and epilepsy after TBI.
If we achieve our goals, they will have a measurable impact on the quality of life of our service personnel, our veterans, and the civilian TBI population.

REFERENCES

1. Bruns, J. & Hauser, W. A. The Epidemiology of Traumatic Brain Injury: A Review. *Epilepsia* **44,** 2–10 (2003).
2. Ghajar, J. Traumatic brain injury. *Lancet* **356,** 923–929 (2000).
3. Rogawski, M. A. Common pathophysiologic mechanisms in migraine and epilepsy. *Arch. Neurol* **65,** 709–714 (2008).
4. D'Ambrosio, R. *et al.* Post-traumatic epilepsy following fluid percussion injury in the rat. *Brain* **127,** 304–314 (2004).
5. Cole, J. T. *et al.* Craniotomy: true sham for traumatic brain injury, or a sham of a sham? *J. Neurotrauma* **28,** 359–369 (2011).
6. Brody, D. L. *et al.* Electromagnetic controlled cortical impact device for precise, graded experimental traumatic brain injury. *J. Neurotrauma* **24,** 657–673 (2007).
7. Herrmann, J. E. *et al.* STAT3 is a critical regulator of astrogliosis and scar formation after spinal cord injury. *J. Neurosci* **28,** 7231–7243 (2008).
8. Aaronson, D. S. & Horvath, C. M. A road map for those who don't know JAK-STAT. *Science* **296,** 1653–1655 (2002).
9. Oliva, A. A., Jr, Kang, Y., Sanchez-Molano, J., Furones, C. & Atkins, C. M. STAT3 signaling after traumatic brain injury. *J. Neurochem.* **120,** 710–720 (2012).
10. Nimmerjahn, A., Kirchhoff, F., Kerr, J. N. D. & Helmchen, F. Sulforhodamine 101 as a specific marker of astroglia in the neocortex in vivo. *Nat Meth* **1,** 31–37 (2004).
11. Appaix, F. *et al.* Specific in vivo staining of astrocytes in the whole brain after intravenous injection of sulforhodamine dyes. *PLoS ONE* **7,** e35169 (2012).
12. Stosiek, C., Garaschuk, O., Holthoff, K. & Konnerth, A. In vivo two-photon calcium imaging of neuronal networks. *PNAS* **100,** 7319–7324 (2003).
13. Tian, L. *et al.* Imaging neural activity in worms, flies and mice with improved GCaMP calcium indicators. *Nat Meth* **6,** 875–881 (2009).
14. Zariwala, H. A. *et al.* A Cre-Dependent GCaMP3 Reporter Mouse for Neuronal Imaging In Vivo. *J. Neurosci.* **32,** 3131–3141 (2012).
15. Hirase, H., Qian, L., Barthó, P. & Buzsáki, G. Calcium Dynamics of Cortical Astrocytic Networks In Vivo. *PLoS Biol* **2,** e96 (2004).
16. Margrie, T., Brecht, M. & Sakmann, B. In vivo, low-resistance, whole-cell recordings from neurons in the anaesthetized and awake mammalian brain. *Pflügers Archiv European Journal of Physiology* **444,** 491–498 (2002).
17. Isaacson, J. S. & Scanziani, M. How inhibition shapes cortical activity. *Neuron* **72,** 231–243 (2011).
18. Kitamura, K., Judkewitz, B., Kano, M., Denk, W. & Häusser, M. Targeted patch-clamp recordings and single-cell electroporation of unlabeled neurons in vivo. *Nat. Methods* **5,** 61–67 (2008).
19. Brennan, K. C. *et al.* Casein kinase iδ mutations in familial migraine and advanced sleep phase. *Sci Transl Med* **5,** 183ra56, 1–11 (2013).
20. Lucas, S., Hoffman, J. M., Bell, K. R., Walker, W. & Dikmen, S. Characterization of headache after traumatic brain injury. *Cephalalgia* **32,** 600–606 (2012).
21. Kinlay, S. Changes in stroke epidemiology, prevention, and treatment. *Circulation* **124,** e494–496 (2011).
22. Roger, V. L. *et al.* Executive summary: heart disease and stroke statistics--2012 update: a report from the american heart association. *Circulation* **125,** 188–197 (2012).
23. Benowitz, L. I. & Carmichael, S. T. Promoting axonal rewiring to improve outcome after stroke. *Neurobiol. Dis.* **37,** 259–266 (2010).
24. Carmichael, S. T. Targets for neural repair therapies after stroke. *Stroke* **41,** S124–126 (2010).
25. Zhang, Z. G. & Chopp, M. Neurorestorative therapies for stroke: underlying mechanisms and translation to the clinic. *Lancet Neurol* **8,** 491–500 (2009).

26.   Clarkson, A. N., Huang, B. S., Macisaac, S. E., Mody, I. & Carmichael, S. T. Reducing excessive GABA-mediated tonic inhibition promotes functional recovery after stroke. *Nature* **468,** 305–309 (2010).

27.   Clarkson, A. N. *et al.* AMPA receptor-induced local brain-derived neurotrophic factor signaling mediates motor recovery after stroke. *J. Neurosci.* **31,** 3766–3775 (2011).

28.   Rammes, G., Danysz, W. & Parsons, C. G. Pharmacodynamics of memantine: an update. *Curr Neuropharmacol* **6,** 55–78 (2008).

29.   Thomas, S. J. & Grossberg, G. T. Memantine: a review of studies into its safety and efficacy in treating Alzheimer's disease and other dementias. *Clin Interv Aging* **4,** 367–377 (2009).

30.   Marvanová, M. *et al.* The neuroprotective agent memantine induces brain-derived neurotrophic factor and trkB receptor expression in rat brain. *Mol. Cell. Neurosci.* **18,** 247–258 (2001).

31.   Meisner, F. *et al.* Memantine upregulates BDNF and prevents dopamine deficits in SIV-infected macaques: a novel pharmacological action of memantine. *Neuropsychopharmacology* **33,** 2228–2236 (2008).

32.   Murphy, T. H. & Corbett, D. Plasticity during stroke recovery: from synapse to behaviour. *Nat. Rev. Neurosci.* **10,** 861–872 (2009).

33.   Minkeviciene, R., Banerjee, P. & Tanila, H. Memantine improves spatial learning in a transgenic mouse model of Alzheimer's disease. *J. Pharmacol. Exp. Ther* **311,** 677–682 (2004).

34.   Kornhuber, J. & Quack, G. Cerebrospinal fluid and serum concentrations of the N-methyl-D-aspartate (NMDA) receptor antagonist memantine in man. *Neurosci. Lett.* **195,** 137–139 (1995).

35.   Grinvald, A., Lieke, E., Frostig, R. D., Gilbert, C. D. & Wiesel, T. N. Functional architecture of cortex revealed by optical imaging of intrinsic signals. *Nature* **324,** 361–4 (1986).

36.   Frostig, R. D., Lieke, E. E., Ts'o, D. Y. & Grinvald, A. Cortical functional architecture and local coupling between neuronal activity and the microcirculation revealed by in vivo high-resolution optical imaging of intrinsic signals. *Proc Natl Acad Sci U S A* **87,** 6082–6086 (1990).

37.   Franklin, K. & Paxinos, G. *The Mouse Brain in Stereotaxic Coordinates.* (Academic Press, 1997).

38.   Rasband, W. S. ImageJ, US National Institutes of Health, Bethesda, Maryland, USA. (1997). at <http://imagej.nih.gov/ij/>

39.   Schallert, T., Fleming, S. M., Leasure, J. L., Tillerson, J. L. & Bland, S. T. CNS plasticity and assessment of forelimb sensorimotor outcome in unilateral rat models of stroke, cortical ablation, parkinsonism and spinal cord injury. *Neuropharmacology* **39,** 777–787 (2000).

40.   Li, X. *et al.* Chronic behavioral testing after focal ischemia in the mouse: functional recovery and the effects of gender. *Exp. Neurol.* **187,** 94–104 (2004).

41.   Kleim, J. A., Boychuk, J. A. & Adkins, D. L. Rat models of upper extremity impairment in stroke. *ILAR J* **48,** 374–384 (2007).

42.   Martinez-Coria, H. *et al.* Memantine improves cognition and reduces Alzheimer's-like neuropathology in transgenic mice. *Am. J. Pathol.* **176,** 870–880 (2010).

43.   Ohab, J. J., Fleming, S., Blesch, A. & Carmichael, S. T. A neurovascular niche for neurogenesis after stroke. *J. Neurosci.* **26,** 13007–13016 (2006).

44.   Myer, D. J., Gurkoff, G. G., Lee, S. M., Hovda, D. A. & Sofroniew, M. V. Essential protective roles of reactive astrocytes in traumatic brain injury. *Brain* **129,** 2761–2772 (2006).

45.   Lapchak, P. A. Memantine, an uncompetitive low affinity NMDA open-channel antagonist improves clinical rating scores in a multiple infarct embolic stroke model in rabbits. *Brain Res.* **1088,** 141–147 (2006).

46.   Babu, C. S. & Ramanathan, M. Pre-ischemic treatment with memantine reversed the neurochemical and behavioural parameters but not energy metabolites in middle cerebral artery occluded rats. *Pharmacol. Biochem. Behav.* **92,** 424–432 (2009).

47.   Sofroniew, M. V. Molecular dissection of reactive astrogliosis and glial scar formation. *Trends Neurosci* **32,** 638–647 (2009).

48.   Ploughman, M. *et al.* Brain-derived neurotrophic factor contributes to recovery of skilled reaching after focal ischemia in rats. *Stroke* **40,** 1490–1495 (2009).

49. Ke, Z., Yip, S. P., Li, L., Zheng, X.-X. & Tong, K.-Y. The effects of voluntary, involuntary, and forced exercises on brain-derived neurotrophic factor and motor function recovery: a rat brain ischemia model. *PLoS ONE* **6,** e16643 (2011).

50. Chen *et al.* Neuroprotective concentrations of the N-methyl-D-aspartate open-channel blocker memantine are effective without cytoplasmic vacuolation following post-ischemic administration and do not block maze learning or long-term potentiation. *Neuroscience* **86,** 1121–1132 (1998).

51. Görgülü, A. *et al.* Reduction of edema and infarction by Memantine and MK-801 after focal cerebral ischaemia and reperfusion in rat. *Acta Neurochir (Wien)* **142,** 1287–1292 (2000).

52. Brown, C. E., Li, P., Boyd, J. D., Delaney, K. R. & Murphy, T. H. Extensive turnover of dendritic spines and vascular remodeling in cortical tissues recovering from stroke. *J. Neurosci.* **27,** 4101–4109 (2007).

53. Chen, H.-S. V. & Lipton, S. A. The chemical biology of clinically tolerated NMDA receptor antagonists. *J. Neurochem* **97,** 1611–1626 (2006).

54. Johnson, J. W. & Kotermanski, S. E. Mechanism of action of memantine. *Curr Opin Pharmacol* **6,** 61–67 (2006).

55. David-Jürgens, M., Churs, L., Berkefeld, T., Zepka, R. F. & Dinse, H. R. Differential effects of aging on fore- and hindpaw maps of rat somatosensory cortex. *PLoS ONE* **3,** e3399 (2008).

56. Brown, C. E., Aminoltejari, K., Erb, H., Winship, I. R. & Murphy, T. H. In vivo voltage-sensitive dye imaging in adult mice reveals that somatosensory maps lost to stroke are replaced over weeks by new structural and functional circuits with prolonged modes of activation within both the peri-infarct zone and distant sites. *J. Neurosci* **29,** 1719–1734 (2009).

57. Klein, A., Sacrey, L.-A. R., Whishaw, I. Q. & Dunnett, S. B. The use of rodent skilled reaching as a translational model for investigating brain damage and disease. *Neurosci Biobehav Rev* **36,** 1030–1042 (2012).

58. Ramanathan, D., Conner, J. M. & Tuszynski, M. H. A form of motor cortical plasticity that correlates with recovery of function after brain injury. *Proc. Natl. Acad. Sci. U.S.A.* **103,** 11370–11375 (2006).

59. Jones, T. A. *et al.* Remodeling the Brain With Behavioral Experience After Stroke. *Stroke* **40,** S136–S138 (2009).

60. Li, S. *et al.* An age-related sprouting transcriptome provides molecular control of axonal sprouting after stroke. *Nat. Neurosci* **13,** 1496–1504 (2010).

61. Matyas, F. *et al.* Motor control by sensory cortex. *Science* **330,** 1240–1243 (2010).

62. Kermani, P. & Hempstead, B. Brain-derived neurotrophic factor: a newly described mediator of angiogenesis. *Trends Cardiovasc. Med.* **17,** 140–143 (2007).

63. Leventhal, C., Rafii, S., Rafii, D., Shahar, A. & Goldman, S. A. Endothelial trophic support of neuronal production and recruitment from the adult mammalian subependyma. *Mol. Cell. Neurosci.* **13,** 450–464 (1999).

64. Qin, L., Kim, E., Ratan, R., Lee, F. S. & Cho, S. Genetic variant of BDNF (Val66Met) polymorphism attenuates stroke-induced angiogenic responses by enhancing anti-angiogenic mediator CD36 expression. *J. Neurosci.* **31,** 775–783 (2011).

65. Prakash, Cohen-Cory, S. & Frostig, R. D. Rapid and opposite effects of BDNF and NGF on the functional organization of the adult cortex in vivo. *Nature* **381,** 702–706 (1996).

66. Li, Y. *et al.* Gliosis and brain remodeling after treatment of stroke in rats with marrow stromal cells. *Glia* **49,** 407–417 (2005).

67. Bacigaluppi, M. *et al.* Delayed post-ischaemic neuroprotection following systemic neural stem cell transplantation involves multiple mechanisms. *Brain* **132,** 2239–2251 (2009).

68. Xia, P., Chen, H. V., Zhang, D. & Lipton, S. A. Memantine preferentially blocks extrasynaptic over synaptic NMDA receptor currents in hippocampal autapses. *J. Neurosci.* **30,** 11246–11250 (2010).

69. Hardingham, G. E. & Bading, H. Synaptic versus extrasynaptic NMDA receptor signalling: implications for neurodegenerative disorders. *Nat. Rev. Neurosci.* **11,** 682–696 (2010).

70. Peeters, M. *et al.* Effects of pan- and subtype-selective NMDA receptor antagonists on cortical spreading depression in the rat: therapeutic potential for migraine. *J Pharmacol Exp Ther* **321,** 564–72 (2007).

71. Sukhotinsky, I. *et al.* Chronic daily cortical spreading depressions suppress spreading depression susceptibility. *Cephalalgia* **31,** 1601–1608 (2011).

72. Lauritzen, M. *et al.* Clinical relevance of cortical spreading depression in neurological disorders: migraine, malignant stroke, subarachnoid and intracranial hemorrhage, and traumatic brain injury. *J. Cereb. Blood Flow Metab.* **31,** 17–35 (2011).

73. Schinder, A. F. & Poo, M. The neurotrophin hypothesis for synaptic plasticity. *Trends Neurosci.* **23,** 639–645 (2000).

74. Nagappan, G. & Lu, B. Activity-dependent modulation of the BDNF receptor TrkB: mechanisms and implications. *Trends Neurosci.* **28,** 464–471 (2005).

75. Sulejczak, D. *et al.* Focal photothrombotic lesion of the rat motor cortex increases BDNF levels in motor-sensory cortical areas not accompanied by recovery of forelimb motor skills. *J. Neurotrauma* **24,** 1362–1377 (2007).

76. Chen, J. *et al.* Endothelial nitric oxide synthase regulates brain-derived neurotrophic factor expression and neurogenesis after stroke in mice. *J. Neurosci.* **25,** 2366–2375 (2005).

77. Molinaro, G. *et al.* Memantine treatment reduces the expression of the K(+)/Cl(-) cotransporter KCC2 in the hippocampus and cerebral cortex, and attenuates behavioural responses mediated by GABA(A) receptor activation in mice. *Brain Res.* **1265,** 75–79 (2009).

78. Al-Amin, H., Sarkis, R., Atweh, S., Jabbur, S. & Saadé, N. Chronic dizocilpine or apomorphine and development of neuropathy in two animal models II: effects on brain cytokines and neurotrophins. *Exp. Neurol.* **228,** 30–40 (2011).

79. Guo, C., Yang, Y., Su, Y. & Si, T. Postnatal BDNF expression profiles in prefrontal cortex and hippocampus of a rat schizophrenia model induced by MK-801 administration. *J. Biomed. Biotechnol.* **2010,** 783297 (2010).

80. Marvanová, M., Lakso, M. & Wong, G. Identification of genes regulated by memantine and MK-801 in adult rat brain by cDNA microarray analysis. *Neuropsychopharmacology* **29,** 1070–1079 (2004).

81. Baumbauer, K. M., Huie, J. R., Hughes, A. J. & Grau, J. W. Timing in the absence of supraspinal input II: regularly spaced stimulation induces a lasting alteration in spinal function that depends on the NMDA receptor, BDNF release, and protein synthesis. *J. Neurosci.* **29,** 14383–14393 (2009).

82. Ninan, I. *et al.* The BDNF Val66Met polymorphism impairs NMDA receptor-dependent synaptic plasticity in the hippocampus. *J. Neurosci.* **30,** 8866–8870 (2010).

83. Chen, L. Y., Rex, C. S., Pham, D. T., Lynch, G. & Gall, C. M. BDNF signaling during learning is regionally differentiated within hippocampus. *J. Neurosci.* **30,** 15097–15101 (2010).

84. Dietrich, W. D. *et al.* Thromboembolic events lead to cortical spreading depression and expression of c-fos, brain-derived neurotrophic factor, glial fibrillary acidic protein, and heat shock protein 70 mRNA in rats. *J. Cereb. Blood Flow Metab.* **20,** 103–111 (2000).

85. Berthier, M. L. *et al.* Memantine and constraint-induced aphasia therapy in chronic poststroke aphasia. *Ann. Neurol.* **65,** 577–585 (2009).